Study on the parameterization response of probabilistic neural networks for seismic facies classification in the Gulf of Mexico

Diana Salazar Florez[1] and Heather Bedle[2]

Abstract

Nowadays, there are many unsupervised and supervised machine learning techniques available for performing seismic facies classification. However, those classification methods either demand high computational costs or do not provide an accurate measure of confidence. Probabilistic neural networks (PNNs) overcome these limitations and have demonstrated their superiority among other algorithms. PNNs have been extensively applied for some prediction tasks, but they have not been well studied regarding the prediction of seismic facies volumes using seismic attributes. We have explored the capability of the PNN algorithm when classifying large- and small-scale seismic facies. In addition, we evaluate the impact of user-chosen parameters on the final classification volumes. After performing seven tests, each with a parameter variation, we assess the impact of the parameter change on the resultant classification volumes. We find that the processing task can have a significant impact on the classification volumes, but we also find how the most geologically complex areas are the most challenging for the algorithm. Moreover, we determine that even if the PNN technique is performing and producing considerably accurate results, it is possible to overcome those limitations and significantly improve the final classification volumes by including the geologic insight provided by the geoscientist. We conclude by proposing a new workflow that can guide future geoscientists interested in applying PNNs, to obtain better seismic facies classification volumes by considering some initial steps and advice.

Introduction

In a previous study, Lubo-Robles et al. (2019) demonstrate the accuracy of the probabilistic neural network (PNN) when classifying seismic facies related to salt and conformable sediments. However, in that study, only two seismic facies were tested and, as geoscientists, we realize that geology can be more complex. For that reason, in this approach, we wanted to test the capability of this novel technique when trying to classify not only large-scale features such as salt, conformable sediments, and mass-transport deposits (MTDs), but also more challenging and subtle, small-scale features such as turbiditic channels, and the noise near the seafloor. In addition, we wanted to explore how including geoscientific insight when defining initial parameters, such as the amount of training data, the seismic attributes preselected, and the preprocessing and conditioning of the data, can influence the final classification models.

For this analysis, we chose the East Breaks and Alaminos Canyon 3D seismic survey located in the Western Gulf of Mexico. This area in the Gulf of Mexico contains a complex geologic setting that consists of architectural elements related to salt domes, hemipelagic sediments, and deepwater deposits such as turbidites and MTDs (Posamentier and Kolla, 2003; Weimer and Slatt, 2006; Galloway, 2008; Posamentier and Martinsen, 2011). All of these elements are present in the seismic volume chosen, which makes it suitable to test the capability of this technique for supervised classification of the seismic facies associated with those architectural elements.

Seismic data

The seismic survey is located in the deepwater Diana intraslope basin between the East Breaks and Alaminos Canyon blocks within the Western Gulf of Mexico (Figure 1). This region includes the important deepwater Diana and Hoover oil and gas fields; therefore, there are also available well data that can be used to validate the geologic facies interpretations. The seismic survey was time -processed and has positive SEG-standard polarity. A full processing report, though, was not publicly available. Due to the necessity of decreasing the high computational cost, the seismic volume was cropped to 325 inlines and 2481 crosslines, with an approximated area of 380 km^2, a record length of 4.1 s, and a bin size of

[1]University of Oklahoma, School of Geosciences, Norman, Oklahoma 73019, USA and Universidad Industrial de Santander, School of Geology, Bucaramanga, Santander 680001, Colombia. E-mail: diana.k.salazar.florez-1@ou.edu (corresponding author).
[2]University of Oklahoma, School of Geosciences, Norman, Oklahoma 73019, USA. E-mail: hbedle@ou.edu.

Manuscript received by the Editor 18 November 2020; revised manuscript received 2 June 2021; published ahead of production 8 August 2021.
This paper appears in *Interpretation*, Vol. 10, No. 1 (February 2022); p. 1–23, 14 FIGS., 3 TABLES.
http://dx.doi.org/10.1190/INT-2020-0218.1.

41 ft^2 × 131 ft^2 × 0.004 s. This cropped region contains a wide variety of geologic features, ideal for the characterization goals of this study.

Geologic setting

By the Middle Jurassic, the invasion of shallow epicontinental seas favored the establishment of restricted environments in which thick sequences of evaporitic sediments were deposited in the graben basins of the Gulf of Mexico (Galloway, 2008; Nixon et al., 2014). The high rates of sediment influx from the Early Cretaceous to Cenozoic, and the consequent sediment load, triggered different events of salt expulsion that formed from salt stock canopy complexes under the continental slope in the Oligocene, to passive diapirism and minibasins in the shelf and slope in the Miocene-Pliocene (Galloway, 2008). In addition, the formation of salt sheets served as decollement zones for basinward gravity spreading and resultant updip extension, which required compensatory compression and created fold belts at the base of the slope such as the Perdido fold belt in the Western Gulf of Mexico (Galloway, 2008). Finally, in the Pleistocene, the rapid Quaternary climate cycling and glacial erosion triggered high rates of sediments that filled the shelf minibasins, whereas the slope minibasins remain unfilled (Galloway, 2008; Nixon et al., 2014).

In the Western Gulf of Mexico, the genesis of the Diana intraslope minibasin may be related to those events of salt expulsion forming diapirism and minibasins in the shelf and slope. The structural configuration observed in the study area is similar to the structural model shown in Figure 3c of Galloway (2008) and is called salt withdrawal minibasins. The Diana minibasin is bounded by two relatively shallow salt bodies and is composed of intercalated sequences of mud-prone MTDs and highstand packages of hemipelagic clays and muds (Donovan et al., 2003; Miller et al., 2012). In the case of these intraslope basins, the MTDs often develop from failure of the delta front and canyon walls during lowstand system track events when the rapid sea-level fall exposes the shelf and slope (Sarkar et al., 2008). According to Sullivan et al. (2000), the turbiditic sandstones, siltstones, and mudstones that comprise the reservoirs in the Diana field were deposited in a lowstand fan within an intraslope subbasin setting.

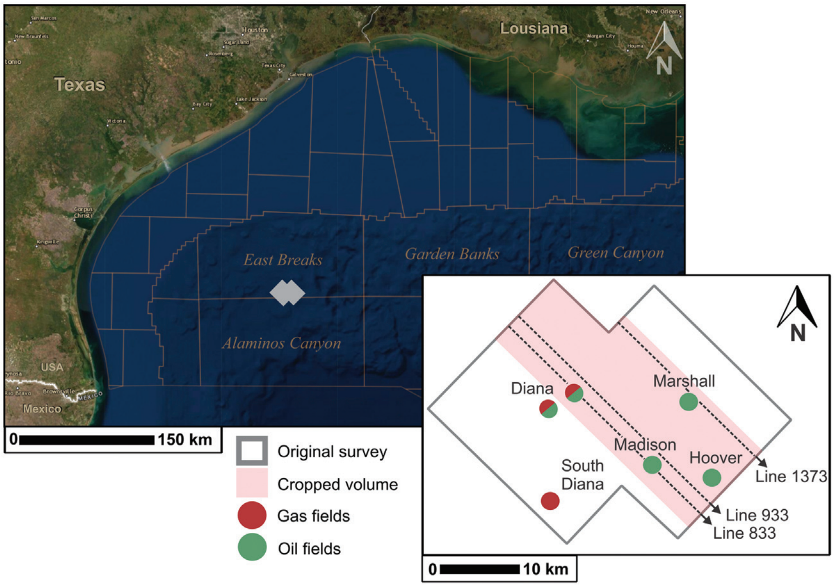

Figure 1. Location of the seismic survey used for this study in the Western Gulf of Mexico. Image modified from the USGS web page.

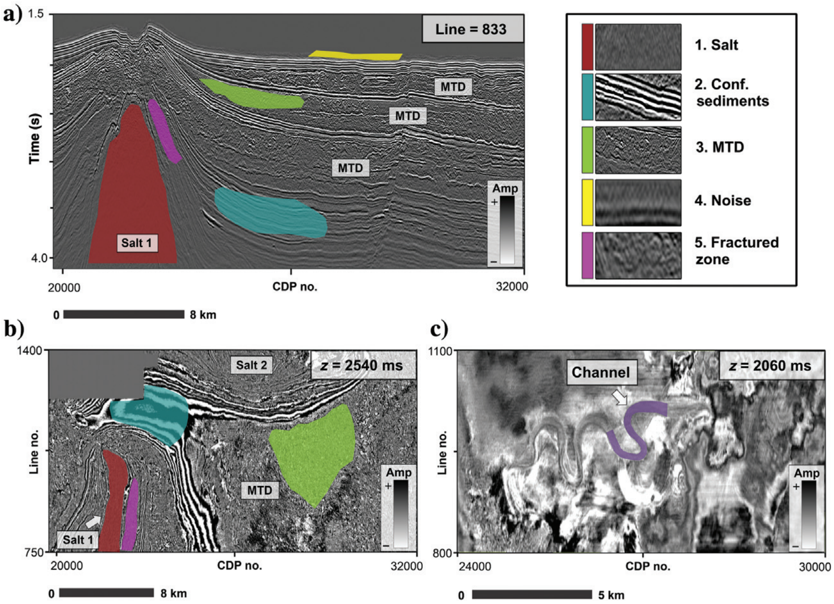

Figure 2. Seismic facies identified and samples of some of the facies polygons picked in the seismic volume for training.

Seismic facies identified

Roksandić (1978) defines seismic facies as a sedimentary unit that is different from the adjacent units in its seismic characteristics: reflection amplitude, dominant reflection frequency, reflection polarity, reflection continuity, reflection configuration, the abundance of reflections, the geometry of the seismic facies unit, and the relationship with other units. Following this concept, we defined five seismic facies shown in Figure 2: (1) salt facies, which are discontinuous, chaotic, and low-amplitude reflectors, (2) conformable sediments facies, composed of continuous, subparallel, and high-amplitude reflectors, (3) MTD facies, characterized by discontinuous, strongly chaotic, and high-amplitude reflectors, (4) noise facies, consisting of continuous, parallel, and low-amplitude reflectors that correspond to the noise near the seafloor, and (5) fractured zone facies, of chaotic, and sometimes semicontinuous, low-amplitude reflectors.

In the amplitude seismic volume, the fractured zone facies were inferred to correspond to conformable sediments and MTDs near the top of the salt dome (the magenta polygons in Figure 2a and 2b). Due to the emplacement of the salt dome, it is possible that most of the nearby strata had been strongly fractured, therefore giving different seismic responses than those strictly related to the conformable sediments and MTD facies. This fifth facies was only included in one of the final tests.

Finally, we also identified a channel (Figure 2c) in the shallow sedimentary strata. To test the capability of the technique when classifying subtle and more challenging features, it was included as a channel facies.

Seismic attributes

In this study, we included six seismic attributes as the initial candidates to perform the PNN classification: the (1) $k1$-most-positive principal curvature, (2) $k2$-most-negative principal curvature, (3) grey level co-occurrence matrix (GLCM) contrast, (4) GLCM dissimilarity, (5) envelope, and (6) coherence.

We included the coherence attribute because it is known to be useful for channel and salt boundary detection (Chopra and Marfurt, 2007a). Regarding the curvature attributes, we included the most-positive curvature $k1$ because it helps to highlight anticlinal and domal features, such as those related to salt domes and channel edges. Alternately, the most-negative curvature $k2$ helps to highlight synclinal and bowl-like features, such as those related to channels axes and withdrawal synclines (Chopra and Marfurt, 2007b). Together, the coherence and the curvature attribute are excellent at delineating seismic stratigraphic features not only related to channels but also related to MTDs (Chopra and Marfurt, 2011). Finally, we included the envelope attribute because it is related to the energy of the trace and helps to detect major and subtle changes in lithology (Taner et al., 1979). In this region, we have a high contrast between the salt lithology and the surrounding sediments (Figure 2a). The same observation can be made between the highstand hemipelagic sediments and the lowstand MTDs with thin intervals of sand-rich turbiditic systems.

Because some geologic features can exhibit curvatures at different wavelengths (Chopra and Marfurt, 2010), we also tested two different ways of calculating the curvature attributes, long-wavelength versus short-wavelength. Short-wavelength estimates of curvature can incorporate dip information of 9–25 traces, whereas the long-wavelength estimates of curvature can use dip information of 400 or more traces (Chopra and Marfurt, 2007b). According to Al-Dossary and Marfurt (2006), long-wavelength estimates of curvature enhance features that are difficult to see using either short-wavelength estimates of curvature or coherence. For this reason, we decided to begin our evaluation by using long-wavelength curvature and after we created a case to evaluate the short-wavelength curvature.

In addition, we included the GLCM attributes in our analysis for many reasons. The first reason is because they help to emphasize internal textures and to better distinguish facies variations (Gao, 2003). Second, GLCM attributes have already been proven in previous PNN studies. West et al. (2002) successfully combine PNN with these types of textural attributes to automate seismic facies classifications. According to Deriche (2016), GLCM-based attributes can differentiate between textures related to salt-dome boundaries and nonrelated textures. In addition, GLCM dissimilarity and GLCM contrast usually show high values for salt facies (Deriche, 2016).

Moreover, we used two additional attributes: the cosine of the instantaneous phase and the dip deviation. The cosine of the instantaneous phase was helpful when picking the facies polygon because it helps to highlight stratigraphic features (Subrahmanyam and Rao, 2008), whereas the dip deviation attribute was only included at the end of this study as part of a final test. The dip deviation is one of the three nonparallelism attributes recently introduced by Qi and Marfurt (2019), which helps to highlight lateral variations of parallelism of reflectors. This attribute was included as an attempt to correct some misclassifications within the conformable facies in areas that were highly faulted due to the emplacement of the salt domes.

Finally, as part of a conditioning step, and as suggested by Qi et al. (2015), we applied the 3D Kuwahara filter on each of the seismic attributes used to perform the PNN algorithm. According to Qi et al. (2015), this type of filter helps to improve seismic facies classifications by smoothing the interior structures while sharpening the edges and, consequently, accomplishing more accurate results. Furthermore, in this study, we tested the impact of using different filter window sizes for classifying large- and small-scale features within our seismic survey.

Methods

Currently, there are several machine learning techniques for classifying seismic facies, from unsupervised methods, such as k-means, self-organizing maps (SOMs), and generative topographic mapping (GTM), to supervised methods, such as support vector machines (SVMs), convolutional neural networks (CNNs), and PNNs. In different studies (Zhao et al., 2015b; Chopra and Marfurt, 2018), these techniques have been compared and contrasted, whereas others (Coléou et al., 2003; Roy et al., 2013; Zhao et al., 2015a) have compared the seismic facies classifications resulting from supervised and unsupervised methods.

According to Zhao et al. (2015b), one of the disadvantages of the k-means algorithm is that it lacks organization, making sample data points that can be related to similar clusters/facies to appear in different ones.

Moreover, this technique requires the definition of a distance, which could be either Euclidean, Mahalanobis, Manhattan, Canberra, or Chebyshev (Barnes and Laughlin, 2002; Chopra and Marfurt, 2018). The definition of the type of distance may have an impact on the classification accuracy and speed (Barnes and Laughlin, 2002). For example, the Euclidean distance works properly when the clusters have a spherical shape, whereas the Mahalanobis distance is more suitable for elliptical shapes (Chopra and Marfurt, 2018). This adds a significant degree of complexity to this unsupervised method. The definition of the distance is not something obvious or intuitive for an unexperienced interpreter and can be an overwhelming decision because it will have a direct impact on the classification performance and results.

In contrast to *k*-means, where the clustering is made over an *N*-dimensional space (Coléou et al., 2003), SOMs and GTM are considered projection techniques or techniques for dimensionality reduction, where the clustering is made over a manifold or deformed 2D surface (Zhao et al., 2015b). According to Chopra and Marfurt (2018), SOMs have several limitations, with the most prominent being that they do not provide a measure of confidence in the final clustering results. This is overcome by the GTM technique, which indicates the cluster that is most likely to be associated with a sample data point, but it also indicates the probability of that specific sample data point belonging to one cluster or another (Zhao et al., 2015b).

Although the unsupervised methods do not use labeled data, they do require a postinterpretation of the classifications made by the algorithm, and sometimes it can be difficult to assign geologic meaning to the automated interpretation (Wrona et al., 2018; Liu et al., 2019). Nevertheless, the supervised methods allow for geologically significant classifications because they are constrained to the number and types of seismic facies previously defined by the geoscientist (West et al., 2002; Wrona et al., 2018). Another advantage of the neural networks used for supervised classification is that they allow for processing considerable amounts of data without excessive memory requirements (Coléou et al., 2003).

Yet, it is important to note that this is not always true for all of the supervised methods. CNNs, although they seem promising as a deep-learning technique that only requires the seismic amplitude volume as input and avoids the necessity of calculating seismic attributes volumes, in fact require large amounts of training data to avoid overfitting and to properly classified the zones not used for training (Waldeland et al., 2018; Di et al., 2019; Liu et al., 2019). In the case of SVMs, because they involve an increase in the dimensionality of the data, they also imply a significant increase in computational cost (Zhao et al., 2015b).

Compared to the other supervised methods, PNNs do not require extensive amounts of training data and their mathematical foundation also trains data sets faster than other multilayer feedforward neural networks (Masters, 1995; West et al., 2002). Moreover, PNNs are not only based on the computation of distance from the input vector to the training vectors, but they are also guided by the quantity of class representatives nearby (Masters, 1995; West et al., 2002). Therefore, PNNs are able to provide a measure of confidence by calculating a probability from one to zero for each sample data point to belong to a class A, B, or C, and finally classifying the sample data point into the category with the highest probability (West et al., 2002). All of these aspects make PNNs a promising technique that can assure geologic meaning, faster training, and accurate classifications with a measure of confidence.

Due to the characteristic of artificial neural networks, such as PNNs, to find nonlinear relationships between well-log data and seismic data, there are several papers that have proven the accuracy of PNNs for predicting reservoir properties (Hampson et al., 2001; Leiphart and Hart, 2001; Pramanik et al., 2004; Putri et al., 2018; Liu et al., 2019). However, there are few papers that have applied PNNs for seismic facies classification (West et al., 2002; Lubo-Robles et al., 2019, 2021). West et al. (2002) present successful results by applying only textural attributes, whereas Lubo-Robles et al. (2019, 2021), despite using different types of seismic attributes, perform the classification of only seismic facies related to salt and conformable reflectors. With the success of those classifications, it is necessary to keep exploring the capabilities of the PNN algorithm by testing it on more complex scenarios using more seismic facies and different types of seismic attributes.

In all of the previous applications of PNNs, the seismic attributes selection for the classification or prediction task has been done by stepwise regression (Hampson et al., 2001; Leiphart and Hart, 2001; Putri et al., 2018), multilinear regression (Mercado-Herrera et al., 2006), or by geoscientist expertise (West et al., 2002; Verma et al., 2012). However, as has been stated by several authors (Barnes and Laughlin, 2002; Zhao et al., 2018; Kim et al., 2019; La Marca-Molina, 2020), the proper selection of the seismic attributes is crucial because it has an important impact on the final results and could be more important than the algorithm itself. Therefore, the last advantage of the PNN algorithm applied in this study is that it is coupled with an exhaustive searching algorithm. The objective of this exhaustive algorithm is to find the best combination of seismic attributes and scaling parameters that allows for the most accurate results. This novel technique was introduced by Lubo-Robles et al. (2019, 2021) under the name exhaustive PNN.

PNN method

To further understand the mathematics behind the PNN method, it is first necessary to clarify a few concepts. Following Lubo-Robles et al. (2021), the seismic volume is separated into (1) training data, (2) validation data, and (3) unseen data. The first two are labeled data used to train/learn the algorithm and finally to test/validate its performance respectively. However, the unseen data are left blind to be fully classified by a trained PNN. Moreover, PNN is a voxel-type classification technique, which means that the training and validation data are selected by the interpreter by picking polygons surrounding samples within the seismic facies of interest. Those samples will consist of values in the N-seismic attributes volumes chosen for the classification task. In this sense, the samples will be vectors of N-components in an N-dimensional space.

The statistical foundation behind the PNN method was proposed by Specht (1988, 1990) and Masters (1995) and was further explained by Lubo-Robles et al. (2019, 2021). PNN is a method for pattern classification based on the Bayes' strategy for decision making and the Parzen method. In the Bayes' strategy, the decision $\boldsymbol{d}(\mathbf{x})$ of classifying a pattern $\mathbf{x}$ as part of a category $\boldsymbol{k}$ or $\boldsymbol{q}$ depends on a probability density function $\boldsymbol{f}(\mathbf{x})$ so that the Bayes's rule will classify a sample $\mathbf{x}$ into a specific category if this category has a higher density of its members around $\mathbf{x}$; otherwise, it will favor the other category (Specht, 1988; Lubo-Robles et al., 2021). Note that the $\mathbf{x}$ pattern corresponds to the vector formed by the N-seismic attribute values:

$$\boldsymbol{d}(\mathbf{x}) = \boldsymbol{q} \quad \text{if } \boldsymbol{f_q}(\mathbf{x}) > \boldsymbol{f_k}(\mathbf{x}), \tag{1}$$

$$\boldsymbol{d}(\mathbf{x}) = \boldsymbol{k} \quad \text{if } \boldsymbol{f_q}(\mathbf{x}) < \boldsymbol{f_k}(\mathbf{x}). \tag{2}$$

The Parzen method is used to estimate the probability density function for each category. In simpler terms, this method calculates a weight function for each training sample point and estimates the density function as a scaled sum of all of the individual weight functions (Figure 3). According to Masters (1995), the best and most common weight function, also called a kernel or potential function, is the Gaussian distribution. In addition to that, in the Parzen approximation, there is also an important scaling parameter $\boldsymbol{\sigma}$that defines the width of the bell-shaped curve that surrounds each sample point and that has a profound effect on the performance of PNN (Figure 3; Masters, 1995).

Mathematically, Lubo-Robles et al. (2021) describe the probability density function of a sample $\mathbf{x}$ to be classified within the category k as follows:

$$f_k(\mathbf{x}) = \frac{1}{T_k}\sum_{t=1}^{T_k} \exp^{\left[-\sum_{i=1}^{I}\frac{(x_i - a_{ti})^2}{\sigma^2}\right]}, \tag{3}$$

where $\boldsymbol{T_k}$ is the number of training samples associated with the kth category defined by the training data, I is the number of input attributes, $\boldsymbol{a_{ti}}$ is the training seismic attribute vector, $\boldsymbol{\sigma}$ is the smoothing parameter, and $\mathbf{x}$ is a validation seismic attribute vector during the training process and an unlabeled sample during the classification.

In addition to the classification volume, the PNN also provides a measure of the classification confidence $\boldsymbol{P_k}(\mathbf{x})$, which represents the probability of a sample $\mathbf{x}$ to be part of a category k. Therefore, if there are three categories/seismic facies, then there will be three probability volumes, one for each category. According to Lubo-Robles et al. (2021), $\boldsymbol{P_k}(\mathbf{x})$ is calculated through the normalization of each probability density function of category k, $\boldsymbol{f_k}(\mathbf{x})$, by dividing it for the sum of all the density functions of all K classes (equation 4):

$$\boldsymbol{P_k}(\mathbf{x}) = \frac{\boldsymbol{f_k}(\mathbf{x})}{\sum_{q=1}^{K}\boldsymbol{f_q}(\mathbf{x})}. \tag{4}$$

In the technique used in this study and within the work presented by Lubo-Robles et al. (2019, 2021), PNN is also coupled with an exhaustive searching algorithm that tests all of the $\boldsymbol{\sigma}$ values in a user-defined interval, but also all of the different possible combinations of the seismic attributes preselected as the training input for classification purposes. With each iteration, it calculates a global validation error value E that helps the interpreter determine which combination of seismic attributes and which $\boldsymbol{\sigma}$ value is the most theoretically accurate and/or optimal according to the algorithm. Basically, the algorithm compares the classification assigned to the validation data by the machine with the classification assigned by the human interpreter since the beginning, so that it can test its performance. The validation error value $\boldsymbol{E}$ is defined as

$$\boldsymbol{E} = \frac{\mathbf{1}}{\boldsymbol{V}}\sum_{v=1}^{V}\boldsymbol{e_k}(\mathbf{x}_v), \tag{5}$$

where $\boldsymbol{V}$ is the number of validation samples and $\boldsymbol{e_k}(\mathbf{x})$ is the error function defined by Masters (1995) as

$$\boldsymbol{e_k}(\mathbf{x}) = [\mathbf{1} - \boldsymbol{P_k}(\mathbf{x})]^2 + \sum_{q \neq k}[\boldsymbol{P_q}(\mathbf{x})]^2. \tag{6}$$

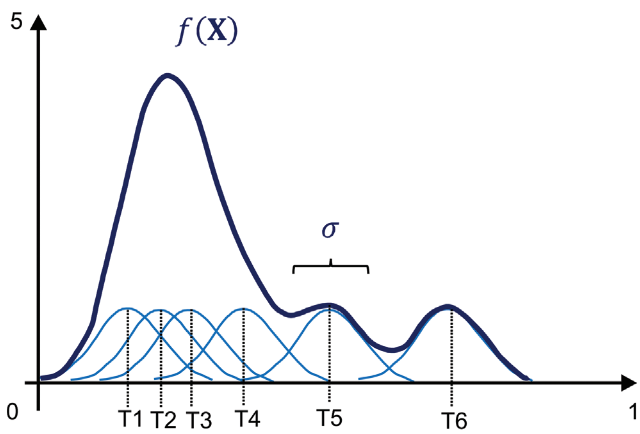

Figure 3. Calculation of the probability density function as a scaled sum of the individual weight functions. The σ value defines the width of the bell-shaped curve that surrounds each sample point. The image is modified from Masters (1995).

If $e_k(\mathbf{x})$ is zero, it means that the validation sample classified by the machine correctly corresponds to the category assigned by the human interpreter. If $e_k(\mathbf{x})$ is one, it means that the validation sample was misclassified in another category (Lubo-Robles et al., 2019). Graphical details regarding the architecture of the PNN and its layers can be found at Lubo-Robles et al. (2021).

Workflow and models

Figure 4 shows the generalized workflow followed in this study. The first part of the workflow involved preparing the input data and preprocessing. These first two steps required picking the polygon facies, selecting and calculating the seismic attributes, and applying the Kuwahara 3D filter. With those two inputs, the training and validation data are generated and labeled. Next, we applied the exhaustive algorithm that provided insight into the combination of attributes and the σ value that has the lowest error E. Theoretically, this value represents the most accurate classification. Finally, the PNN algorithm was applied to generate the facies prediction volume and a probability volume for each seismic facies.

However, because we wanted to study the influence of the parameterization in the final classifications and how they can be improved, we incorporated an additional step, the geoscientist evaluation. It is noteworthy to clarify that the PNN structure remains the same; all of the parameters strictly associated with the algorithm, such as the transformation parameter used to normalize or scale the seismic attributes, the analysis window used to calculate the seismic attributes, and the interval of σ values tested, remained all the same to avoid any biased result and to only test the parameters controlled or chosen by the geoscientist.

In the geoscientist evaluation step, then, we carefully looked at the facies prediction and probability volumes and we identified the misclassified areas and the possible reasons that may have caused them. Afterward, we evaluated the possibility of changing one initial parameter to improve the classification model. Following that analysis, we again applied the algorithms, and we compared these results to understand the impact of each parameter and the limitations of the PNN algorithm.

As mentioned previously, the seismic volume chosen for this study has architectural elements related to the small- and large-scale features. To fulfill the objective of testing the capability of PNN for classifying these architectural elements, we defined three initial models. Model 1 included seismic facies related to the channel, noise, salt, MTD, and conformable sediments; model 2 included the channel, salt, MTD, and conformable sediments facies; and model 3 included only the salt, MTD, and conformable sediment facies.

We applied the generalized workflow several times, changing a specific parameter in each iteration and evaluating the different results obtained for each model. In the end, we had a total of seven tests that will be explained later in this section. First, we need to discuss the specific parameters that the geoscientist can control.

Parameters

The geoscientist can control the following parameters.

Seismic attributes selected

The amount and type of seismic attributes preselected as candidates to perform the PNN classifications will depend on the literature review and geoscientist experience. There are different types of seismic attributes in one category, such as the envelope and instantaneous frequency as instantaneous attributes or chaos and the GLCM as textural attributes. This must be reviewed in the beginning, so that the interpreter will choose the attributes that will best differentiate the seismic facies to be classified.

Moreover, there are different ways to calculate some other attributes, such as the geometric attributes. The coherence attribute can be calculated either as an outer product similarity or a Sobel filter similarity, and the curvature attributes can be calculated as a structural curvature with a long or short wavelength. The interpreter must keep these options in mind.

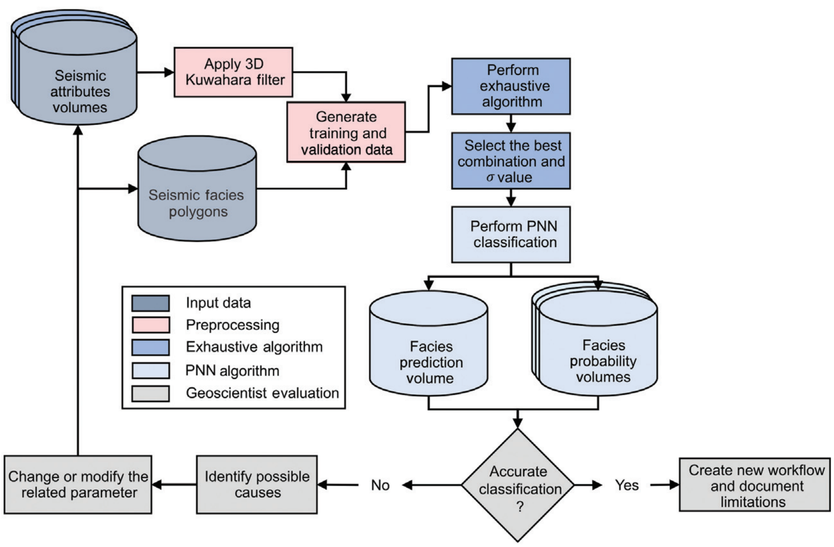

Figure 4. Generalized workflow followed in this study. Here, we included an additional step, the geoscientist criteria, to evaluate the results after applying the PNN algorithm. Modified from Lubo-Robles et al. (2019).

Training and validation data

This subsection corresponds to the way in which the geoscientist will pick the facies polygons to train the algorithm later. The geoscientist can either decide between picking the facies polygons in one, two, or more lines and slices but can also decide on picking in the most straightforward zones or in the most difficult ones. These decisions will have an impact on the time spent in the classifications. Picking more polygons implies more time not only for the interpreter but especially for the machine. Furthermore, picking in challenging zones implies a higher level of difficulty and therefore more time spent by the interpreter.

Finally, this parameter also involves the way in which the geoscientist chooses which polygons will be used for training, which ones will be used for validation, and what part of the volume will be left as unlabeled/tested. Some interpreters may not pay attention to this, but it is an important detail. Training data are exactly for the purpose of training, whereas the validation data are only used for verification and estimation of the error. This means that the algorithm will not learn from the validation polygons, but only from the training polygons.

Seismic facies included

In this parameter, the geoscientist first needs to look at the seismic volume and identify the seismic facies. The seismic facies can be either related to large-scale features or small-scale and subtle features. If both are present, then they must decide between including all of them or just consider classifying some of them.

Seismic volume size

Seismic volumes can be considerably large; therefore, they have a high computational cost. For that reason, the interpreter can decide on using a seismic volume that covers all of the seismic facies of interest or can crop the volume into multiple zones, such as a shallow and a deep zone. For example, this technique is used when generating velocity models. It can also be used to further delineate zones where certain types of geologic features or noise are more likely present.

Analysis window

This parameter generally applies for all of the seismic attributes. However, it is especially important for application of the 3D Kuwahara filter. According to Qi et al. (2016), if the analysis window of the 3D Kuwahara filter is large, the image will be smoother but somewhat blocky, and if the analysis window is small, the image will be less smooth and blockiness will be reduced.

Tests

Now that the parameters have been defined and explained, we can address the individual relations between the parameters and the tests. For each test, we altered a specific parameter that could be either the training data, the analysis window, the volume size, the seismic attributes, or the facies included.

1) Test 1: corresponded to the very first classifications run as starting point
2) Test 2: explored the impact of adding more training data
3) Test 3: changed the size of the analysis window of the 3D Kuwahara filter
4) Test 4: separated the volume into smaller portions
5) Test 5: calculated the curvature attributes using short instead of long wavelength
6) Test 6: included more facies and changed the way of picking the facies polygons
7) Test 7: performed the classification using another seismic attribute, the dip deviation attribute, and explored the generation of training data in the more complex area of the second salt dome.

Figure 5 systematically displays the way in which the tests were run and the logical connections from one test to another. Those connections between tests indicate the way in which a positive impact from a previous test influenced the next one, so that the classifications were progressively improved from one test to another. Notice that some of the tests were addressed in different ways and, for that reason, they may have two or three cases. The specific parameters applied in every test are shown in detail in Table 1.

Test 1: Initial results

We began the first test by picking the facies polygons in one line and one slice for the training data and another line and another slice for the validation data, and the rest of the volume is left unlabeled. In this test, we applied the 3D Kuwahara filter with an analysis window equal to the default bin size of 41 $ft^2 \times 131\ ft^2 \times 0.004$ s. We also used the entire, initially cropped volume with a record length of 4.1 s. This first test served as a starting

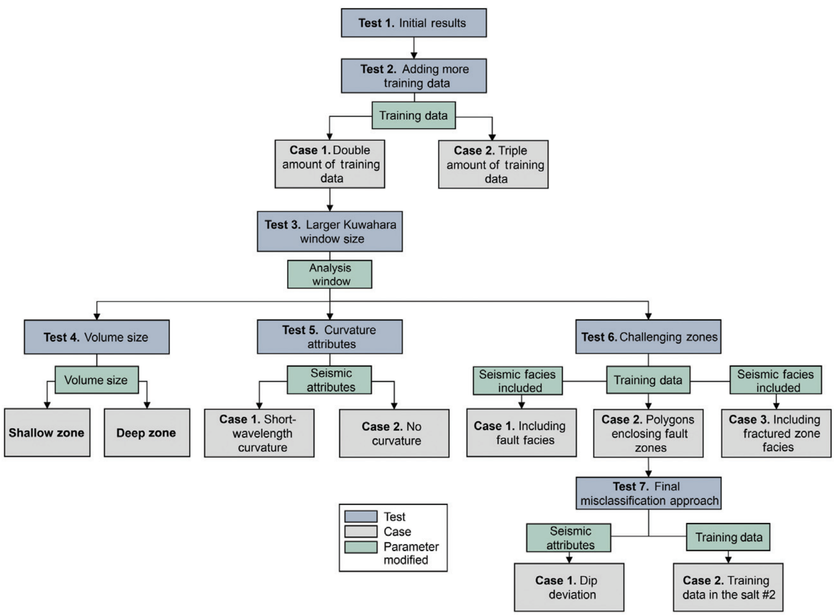

Figure 5. Tests and cases run in this study and the connections between them. The green boxes also indicated the specific parameter modified in each case. Notice that the process was not fully continuous: There were cases that influenced later ones, whereas there were others that did not.

Table 1. Specific parameters applied for every test and case.

Test	Parameter modified	Objective	Case	Specific parameters: Seismic attributes preselected	Amount of training data	3D Kuwahara analysis window size	Seismic facies included	Volume size (record length) (s)
Test 1	—	Initial results	—	$k1$ and $k2$ (long wavelength), GLCM contrast, GLCM dissimilarity, envelope, and coherence	One line, one slice	41 $ft^2 \times 131$ $ft^2 \times 0.004s$	Salt, MTD, conf. sediments, channel, and noise	1.5–4.1
Test 2	Training data	Test the impact of adding more training data	Case 1		Two lines, two time slices	41 $ft^2 \times 131$ $ft^2 \times 0.004$ s	Salt, MTD, conf. sediments, channel, and noise	1.5–4.1
			Case 2		Three lines, three time slices	41 $ft^2 \times 131$ $ft^2 \times 0.004$ s	Salt, MTD, and conf. sediments	1.5–4.1
Test 3	Analysis window	Test the impact of increasing the analysis window for the calculation of the 3D Kuwahara filter	—		Two lines, two time slices	123 $ft^2 \times 393$ $ft^2 \times 0.012$ s	Salt, MTD, conf. sediments, channel, and noise	1.5–4.1
Test 4	Cropping the volume	Use smaller volumes to verify any possible improvement in the facies prediction volumes	Shallow		Two lines, two time slices	41 $ft^2 \times 131$ $ft^2 \times 0.004$ s 123 $ft^2 \times 393$ $ft^2 \times 0.012$ s	Salt, MTD, conf. sediments, channel, and noise	1.5–2.7
			Deep		Two lines, two time slices	123 $ft^2 \times 393$ $ft^2 \times 0.012$ s	Salt, MTD, and conf. sediments	2.6–4.1
Test 5	Attributes selected	Change the way of calculating the curvature attributes to possibly eliminate or diminish the response of vertical artifacts	Case 1	$k1$ and $k2$ (short wavelength), GLCM contrast, GLCM dissimilarity, envelope, and coherence	Two lines, two time slices	123 $ft^2 \times 393$ $ft^2 \times 0.012$ s	Salt, MTD, and conf. sediments	1.5–4.1
			Case 2		Two lines, two time slices	123 $ft^2 \times 393$ $ft^2 \times 0.012$ s	Salt, MTD, and conf. sediments	1.5–4.1
Test 6	Facies included	Add a fault facies to classify the faults and eliminate misclassifications in those areas	Case 1	$k1$ and $k2$ (long wavelength), GLCM contrast, GLCM dissimilarity, envelope, and coherence	Two lines, two time slices	123 $ft^2 \times 393$ $ft^2 \times 0.012$ s	Salt, MTD, conf. sediments, and faults	1.5–4.1
	Training data	Test the impact of changing the way of picking the facies polygons in faulted zones	Case 2		Two lines, two time slices	123 $ft^2 \times 393$ $ft^2 \times 0.012$ s	Salt, MTD, and conf. sediments	1.5–4.1
	Facies included	Add a fractured zone facies to classify the highly fractured strata around the tops of the salt domes	Case 3		Two lines, two time slices	123 $ft^2 \times 393$ $ft^2 \times 0.012$ s	Salt, MTD, conf. sediments, and fractured zone	1.5–4.1
Test 7	Attributes selected	Test a nonparallelism attribute to better classify conformable sediments facies, especially in zones where those facies are highly fractured	Case 1	$k1$ and $k2$ (long wavelength), GLCM contrast, GLCM dissimilarity, envelope, and dip deviation	Two lines, two time slices	123 $ft^2 \times 393$ $ft^2 \times 0.012$ s	Salt, MTD, and conf. sediments	1.5–4.1
	Training data	Test the impact of changing the way of picking the facies polygons in more complex zones	Case 2	$k1$ and $k2$ (long wavelength), GLCM contrast, GLCM dissimilarity, envelope, and coherence	Two lines, two time slices	123 $ft^2 \times 393$ $ft^2 \times 0.012$ s	Salt, MTD, and conf. sediments	1.5–4.1

point to detect the initially misclassified zones and to begin making modifications to the initial parameters.

Test 2: Training data

In test 2, we wanted to explore the impact of adding more training data. This parameter can help improve the seismic facies classification, but it can also lead to higher computational costs. We then created two cases. Case 1 had double the amount of training data, and it means two lines and two slices. Case 2 used triple the amount of training data, which means three lines and three slices. The rest of the parameters remained the same. With this test, we would be able to see how worthy it would be to increase the training data, and, if so, how big should that increase be. The first case was tested with the three models, whereas the second case used model 3 only. The new included facies polygons were all picked in the first salt-dome area.

Test 3: 3D Kuwahara filter window

For test 3, we explored the impact of using a larger analysis window when applying the 3D Kuwahara filter on the seismic attributes. We applied an analysis window of 123 $ft^2 \times 393$ $ft^2 \times 0.012$ s. According to Qi et al. (2015), this may help to better define the seismic facies. However, in those studies, it was considered only for large-scale features, whereas in our models, there are small- and large-scale facies. Therefore, it was necessary to evaluate the impact of changing this filter parameter on each model.

Test 4: Volume size

Following the assumption that using a smaller volume can make it easier for the algorithm to classify the seismic facies of interest, we decided to explore that possibility by cropping the seismic volume into a shallow and a deep part in test 4. The shallow part covered the region between 1.5 and 2.7 s, whereas the deep part covered the interval from 2.6 to 4.1 s. The classification for the deep portion was only run for the model 3 because the only facies encountered within this interval are the salt, MTD, and conformable sediments. However, the shallow part was run for all three models because in this region there are the channel, noise, salt, MTD, and conformable sediment facies.

Test 5: Curvature attributes

When running the previous classifications, we noticed some vertical artifacts within all of the seismic facies classification models. We related those vertical artifacts to the curvature attributes calculated with a long wavelength. In case 1 of test 5, we decided to test the possibility of using a short wavelength instead, whereas in case 2, we did not use any of the curvature attributes. We ran these cases only using model 3. In this sense, with test 5, we could analyze the impact of changing the way of calculating seismic attributes, such as the curvature attributes.

Test 6: Challenging zones

To address challenging areas, such as the highly faulted areas and the fractured zones, we explored three cases in test 6. Case 1 included fault facies, case 2 used facies polygons that enclose the faulted zones, and case 3 included fractured zone facies. All of those facies were picked near the first salt-dome area.

Test 7: Final misclassifications approach

Finally, in test 7, we wanted to improve some misclassified areas between the conformable sediments and the MTD facies that were especially seen near the second salt dome. To do so, in case 1, we decided to perform the seismic facies classification using the dip deviation attribute instead of the coherence attribute. In case 2, we changed the way of picking the facies polygons and, therefore, the way of training the data. In this case 2, we decided to pick the facies polygons near the second salt-dome area, where the conformable sediments were highly faulted and where the intercalations between the MTDs and the conformable sediments were more difficult to distinguish. In addition, with this case 2, we wanted to determine whether the seismic facies classifications would improve significantly when training in the more difficult areas.

Results

In this section, we analyze the results obtained from each individual test after changing a specific parameter. For this analysis, we compared the outcomes of a specific test with the outcomes of the previous one. We evaluated the results of each test by performing a detailed analysis of the resultant facies classification volumes provided by the PNN algorithm, as well as by examining the error calculated by the exhaustive algorithm. As mentioned previously, this error is calculated through the internal comparison of the classification assigned to the validation data by the machine and the classification assigned by the interpreter during the training process. In this section, we will also present how the results of the early tests and cases influenced the parameter definition of later ones. Table 2 shows a compilation of the best combinations of attributes and sigma values obtained from every test and case. Notice that the $k1$-most-positive principal curvature, envelope, and the coherence attribute comprised almost all of the best combinations calculated by the exhaustive algorithm to perform the seismic facies classification. The second case of the last test 7 was the only exception. Also, note that most of the sigma values are between 0.1 and 0.3.

Regarding the computational effort to perform all of these classifications, the algorithm took less than 10 s for generation of the training data, whereas the time for the exhaustive search algorithm to find the best combination among the 63 possible at every test varied between 3 and 10 min, depending on the number of facies polygons. When applying the PNNs, the time varied between 30 min and a maximum of 2 h, which was during classifying all of the five seismic facies, the double of the polygons, and using the combination of four attributes. The server used consisted of 120 threads and 256 GB of memory; however, because it was a shared environment, only 40 threads were used in every process.

Test 1: Initial results

Model 1 used the following combination of seismic attributes: $k1$, GLCM dissimilarity, envelope, and coherence, with a σ value of 0.1. This combination showed the lowest error value of 0.274. In these results (Figure 6a), we can notice the misclassifications of salt, MTD, and noise facies, into the conformable sediments of the deeper parts of the volume. There were also some misinterpretations in the conformable sediment layers that were classified as channel facies. However, observe that the algorithm distinguished the noise layer at the top of the section quite well despite the misclassifications at the bottom. When looking at time slice 2060 ms, where we should clearly see the channel (Figure 6a), we notice that it was in fact correctly classified into the corresponding facies and was isolated from the surrounding conformable sediments facies. Other areas in the same time slice, though, were incorrectly classified as channel facies.

Model 2 had the lowest error value of 0.233 with a σ value of 0.1 and the following combination of seismic attributes: $k1$, envelope, and coherence. Similar to the results of previous model 1, the algorithm struggled to differentiate the salt from the MTD facies in the deep part of the seismic volume and the top of the salt dome (Figure 6b). In addition, some areas related to conformable sediments facies were misclassified as channel facies. In time slice 2060 ms, the channel was better defined and isolated compared to model 1 (Figure 6b). However, notice that other areas were misinterpreted as channel facies and also had stronger responses. This indicates that the correct and incorrect classifications of the channel facies in model 1 were better highlighted in model 2.

Table 2. Compilation of the best combinations of seismic attributes and σ values obtained from every test and case.

Test	Case	Model	Seismic facies	Best combination	Error	Sigma
Test 1	N/A	1	Salt, MTD, conf. sediments, channel, and noise	$k1$, GLCM dissimilarity, envelope, and coherence	0.274	0.1
		2	Salt, MTD, conf. sediments, and channel	$k1$, envelope, and coherence	0.233	0.1
		3	Salt, MTD, and conf. sediments	$k1$, envelope, and coherence	0.147	0.2
Test 2	Case 1	1	Salt, MTD, conf. sediments, channel, and noise	$k1$, GLCM contrast, envelope, and coherence	0.233	0.1
		2	Salt, MTD, conf. sediments, and channel	$k1$, envelope, and coherence	0.199	0.1
		3	Salt, MTD, and conf. sediments	$k1$, envelope, and coherence	0.148	0.1
	Case 2	3	Salt, MTD, and conf. sediments	$k1$, envelope, and coherence	0.143	0.1
Test 3	N/A	1	Salt, MTD, conf. sediments, channel, and noise	$k1$, $k2$, GLCM contrast, envelope, and coherence	0.181	0.2
		2	Salt, MTD, conf. sediments, and channel	$k1$, GLCM contrast, envelope, and coherence	0.136	0.2
		3	Salt, MTD, and conf. sediments	$k1$, GLCM contrast, envelope, and coherence	0.092	0.2
Test 4	Shallow	1	Salt, MTD, conf. sediments, channel, and noise	$k1$, envelope, and coherence	0.302	0.1
		2	Salt, MTD, conf. sediments, and channel	$k1$, envelope, and coherence	0.277	0.1
		3	Salt, MTD, and conf. sediments	$k1$, envelope, and coherence	0.145	0.1
	Deep	3	Salt, MTD, and conf. sediments	GLCM dissimilarity, envelope, and coherence	0.081	0.1
Test 5	Case 1	3	Salt, MTD, and conf. sediments	$k1$ (short wavelength), GLCM contrast, envelope, and coherence	0.113	0.2
	Case 2	3	Salt, MTD, and conf. sediments	GLCM contrast, envelope, and coherence	0.11	0.2
Test 6	Case 1	—	Salt, MTD, conf. sediments, and faults	$k1$,$k2$, GLCM dissimilarity, envelope, and coherence	0.108	0.3
	Case 2	3	Salt, MTD, and conf. sediments	$k1$, GLCM contrast, envelope, and coherence	0.102	0.2
	Case 3	—	Salt, MTD, conf. sediments, and fractured zone	$k1$, envelope, and coherence	0.239	0.1
Test 7	Case 1	3	Salt, MTD, and conf. sediments	$k1$, GLCM contrast, envelope, and dip deviation	0.111	0.2
	Case 2	3	Salt, MTD, and conf. sediments	$k2$, envelope, and coherence	0.103	0.2

Model 3, classifying only large-scale features related to salt, MTDs, and conformable sediments, had the lowest error value of 0.147 using a σ value of 0.2 and had the following combination of seismic attributes: $k1$, envelope, and coherence. In the deep zones of the seismic volume, we can notice that the algorithm had difficulties distinguishing between salt and MTD facies and between salt and conformable sediments (Figure 6c).

Notice that in all the three models, the area that we interpreted as a highly fractured zone was classified as salt. Also, note that most of the misclassifications have a vertical artifact pattern. We then decided to increase the amount of training data in the second test, seeking for an improvement of the classifications in those troubling zones.

Test 2: Training data

In the first case, when using double the amount of training data, model 1 had its lowest error value of 0.233 with a σ value of 0.1 and the attribute combination of $k1$, GLCM contrast, envelope, and coherence. Note that the misclassifications within the deep zones decreased considerably (Figure 7a), whereas the ones in the shallow portion remained almost the same. The channel in time slice 2060 ms was subtly more highlighted, and the misclassified noise facies were less obvious when compared with test 1.

Model 2 had the lowest error value 0.199 when applying a σ value of 0.1 and using an attribute combination of $k1$, envelope, and coherence. The misclassifications between the channel and the conformable sediments (Figure 7b) remained nearly the same when compared with the results from test 1. However, the channel was better highlighted and isolated in time slice 2060 ms of test 2.

For the first case, model 3 had the most optimal and lowest error value of 0.148 when combining $k1$, envelope, and coherence and applying a σ value of 0.1. In Figure 7c, we can evidence a considerable classification improvement in the deep zones of the seismic volume after doubling the amount of training data. However, the second case of model 3 did not show any noticeable difference after using triple the amount of training data (Figure 7d).

Some similar observations in all the three models were the general decrease in the lowest error value, fewer misclassifications between the salt and the MTD facies in the deep parts of the seismic volume, and the fractured zone near the top of the salt domes being mostly classified as MTD facies. Also, notice that, in all of the models, the fault zones remained being misclassified and we can still observe the vertical artifacts.

Overall, after using double the amount of training data, the results improved considerably. Yet, when using triple the amount of training data, the classification did not show any significant improvement, while actually having a higher computational cost.

Test 3: 3D Kuwahara filter window

For this test, we decided to use a larger analysis window of 123 $ft^2 \times 393$ $ft^2 \times 0.012$ s. Following the results obtained from the previous test 2, we also decided to continue using double the amount of training data because it performed better and generated more accurate results. The rest of the parameters remained the same.

Model 1 had the most optimal error value of 0.181 when applying σ equal to 0.2 and combining $k1$, $k2$, GLCM contrast, envelope, and coherence. Model 2 had the most optimal error value of 0.136 with σ equal

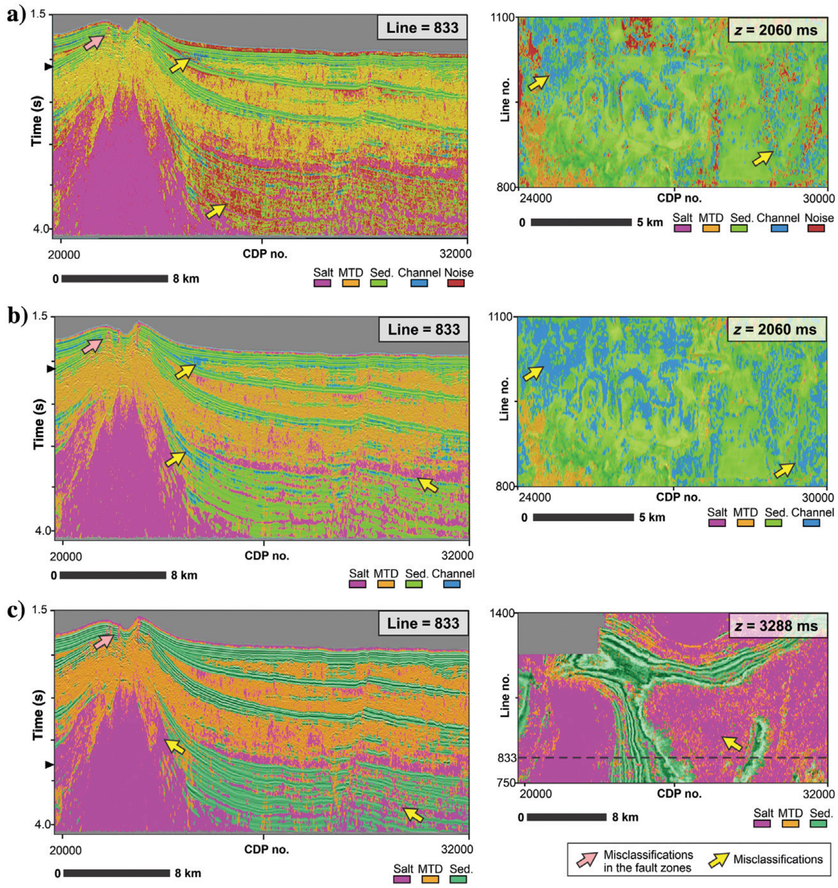

Figure 6. Facies prediction volumes obtained from test 1 after training the algorithm with one line and one time slice and applying a 3D Kuwahara filter equal to the default bin size. (a) Model 1, (b) model 2, and (c) model 3. Notice that, in the three models, the deep part is being misclassified either as salt, channel, or noise facies. In model 1, notice that the noise layer was well classified and in time slice at 2060 ms the channel was correctly interpreted into its corresponding facies. In model 2, the channel is better highlighted. In model 3, the time slice at 3288 ms showed an MTD being misclassified as salt. All of the images correspond to the corender of the amplitude volume and the facies prediction volumes.

to 0.2 and using $k1$, GLCM contrast, envelope, and coherence. This attribute combination and σ value were also the most optimal for model 3, which had an error value of 0.092.

After changing this parameter, the results for the three models improved considerably for the seismic facies related to large-scale features. In Figure 8, we can notice a misclassification decrease between the MTD and the salt facies and inside the conformable sediments present within the deep zones for all three models. In this test, model 3 (Figure 8c) noticeably stood out when compared with the previous classifications.

In time slice 2060 ms of models 1 and 2, the channel is hardly seen now (Figure 8a and 8b). Yet, the noise layer near the seafloor in model 1, despite being well interpreted, extended to the shallow parts of the conformable sediment facies, rendering the overall result inaccurate (Figure 8a). The misclassified faulted zones were not corrected in either of the models.

After these results, which appeared only to be suitable for model 3, we decided to run the next tests by increasing the 3D Kuwahara filter window size for model 3 only, while keeping a small filter analysis window for the other models.

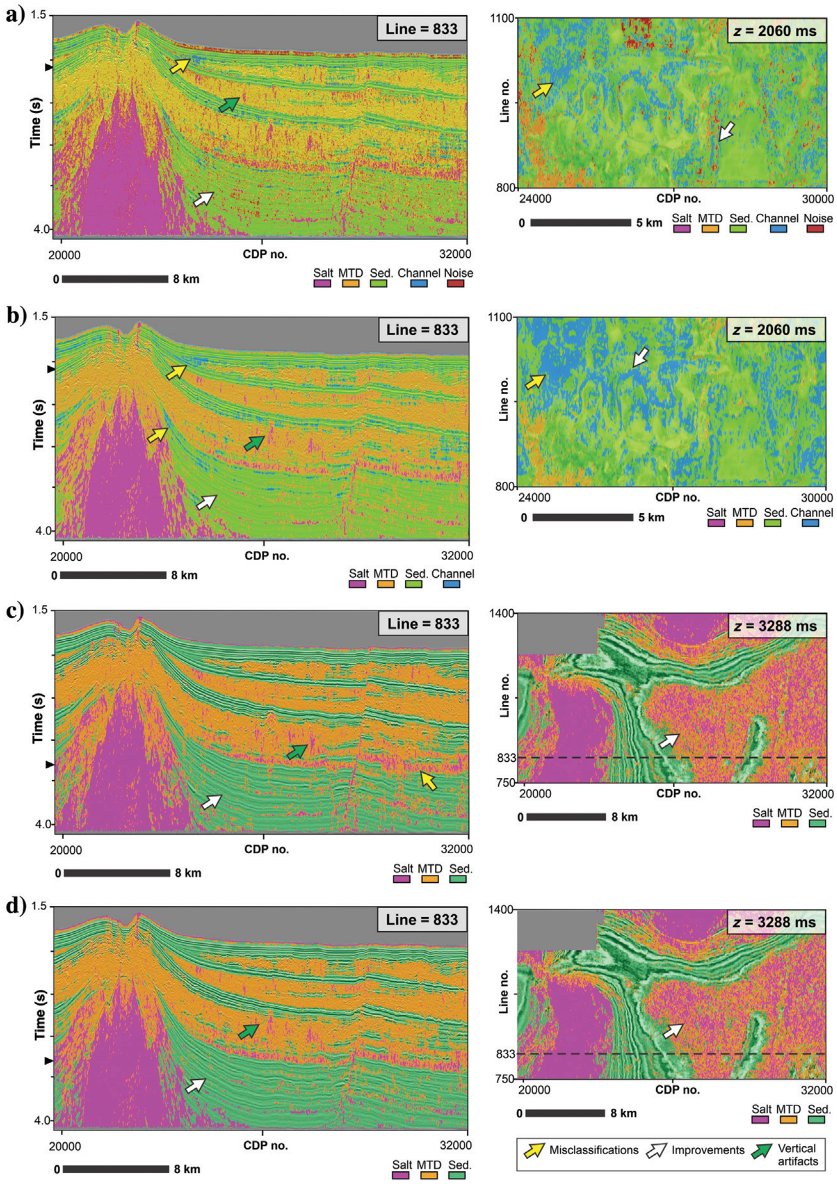

Figure 7. Facies prediction volumes obtained from test 2 after increasing the amount of training data. (a-c) Model 1, model 2, and model 3, respectively, when using double the amount of training data. (d) Model 3 when using triple the amount of training data. Notice the considerable decrease of misclassifications in the deep portion of the facies prediction volumes when using double the amount of training data, whereas when using triple the amount of training data, there was not a significant improvement.

Test 4: Volume size

In this test, we cropped the seismic volume into a shallow and a deep portion. The shallow portion was run for the three models, whereas the deep portion was only run for model 3. This is because there are only large-scale features present in the deep region; therefore, it is only necessary that the model focuses on those.

The shallow zone of model 1 had the lowest error value of 0.302 with σ equal to 0.1 and using the attribute combination of $k1$, envelope, and coherence. This error value is larger than the error value obtained for model 1 in test 2, which used the entire volume. When comparing the classifications in the shallow part of test 2 (Figure 7a) and test 4 (Figure 9a), there are more misclassifications after cropping the volume. These misclassifications are especially present within the MTD facies where the vertical artifacts are more noticeable. In time slice 2060 ms (Figure 9a), the channel and other misclassifications were also more highlighted.

The results obtained for model 2 were similar to those obtained for model 1. The lowest error value of 0.277 was also larger than the value obtained for model 2 in test 2, and it was achieved with σ equal to 0.1 and using the $k1$, envelope, and coherence attributes. Figure 9b shows the increase of misclassifications inside the MTD facies, which showed vertical artifacts. In addition, in the time slice of Figure 9b, we notice that there is no significant improvement between the classification of the channel in test 4 when compared to test 2.

The shallow region of model 3 (Figure 9c) had the most optimal error value of 0.145 with σ equal to 0.1 and using the $k1$, envelope, and coherence attributes. The deep portion had the lowest error value of 0.081 using the GLCM dissimilarity, envelope, and coherence attributes, and σ of 0.1. The shallow part exhibited the same artifacts seen in models 1 and 2 (Figure 9a and 9b). In the deep part, the main difference compared to the previous tests was that the zones near the salt body were interpreted as MTDs instead of salt (Figure 9d). In time slice 3288 ms of model 3, the MTD and salt facies were well distinguished and showed results similar to those obtained from test 3.

Test 5: Curvature attributes

The objective of this test was to suppress or diminish the vertical artifacts observed in the previous tests. We created two cases: Case 1 changed the curvature attributes calculated with a long wavelength with curvature attributes calculated with a short wavelength and case 2 did not include curvature attributes. We ran these cases for the classification of facies of model 3 only.

Until this point, the most accurate classification obtained for model 3 was the one obtained from test 3. In that classification of facies, model 3 had the most optimal error value of 0.092 with the combination of the $k1$ (long wavelength), GLCM contrast, envelope, and coherence attributes (Figure 8c). To have an unbiased comparison, we performed the classification using the same combination of attributes but with the $k1$ calculated with a short wavelength. This combination had an error value of 0.113 using σ equal to 0.2. Despite some remaining misclassified areas inside the MTD and conformable sediments facies, the vertical pattern was successfully suppressed from the artifacts and the misclassifications in the faulted zones were not as strong (Figure 10a). Using the $k1$ (short wavelength), though, had an impact on the top of the salt body that is not as well defined as when using $k1$ (long wavelength).

Figure 10b shows the second case that we tested, which did not use either of the curvature attributes. To also have an unbiased comparison, in this case, we performed the classification by excluding the $k1$ attribute and only using the GLCM contrast, envelope, and coherence attributes. According to the exhaustive algorithm, this combination had the lowest error value of 0.110 with σ equal to 0.2. In this case, the misclassification in the fault zones and the vertical patterns were completely suppressed (Figure 10b). Nevertheless, just as in the previous case when using $k1$ (short wavelength), the top of the salt body was not well-defined.

Not wanting to sacrifice the top of the salt dome by suppressing the vertical artifacts, we reviewed the different possibilities to address this situation. We decided to revisit some of the initial parameters that the geoscientist can control, such as the facies polygons and the training data. We then decided to make another test considering those parameters and those challenging classification zones.

Test 6: Challenging zones

In this test, we ran three different cases. Case 1 included a fault facies (Figure 11a), case 2 created polygons of facies that enclose the faulted zones (Figure 11b), and case 3 included a fractured zone facies (Figure 11c).

For the first case, we created another model to classify the salt, MTD, conformable sediments, and fault facies. We ran the classification using a filter analysis window size of 123 ft^2 × 393 ft^2 × 0.012 s and picked two lines and two slices for the training data. We performed the classification with a σ value equal to 0.3 and using the $k1$ and $k2$ (long wavelength), GLCM dissimilarity, envelope, and coherence attributes. This attribute combination had an error value of 0.108. Despite

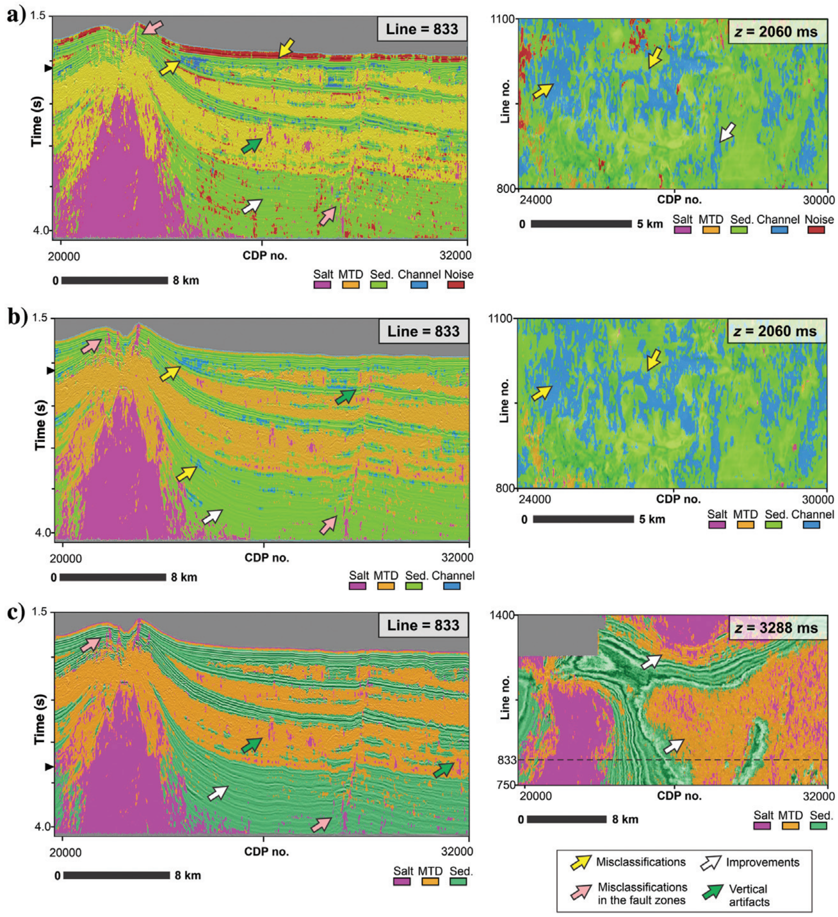

Figure 8. Facies prediction volumes obtained from test 3 after using double the amount of training data and a larger analysis window for the calculation of the 3D Kuwahara filter. (a) Model 1, (b) model 2, and (c) model 3. Notice that, in all three models, the classification of large-scale features was better performed whereas the classification of small-scale features was degraded. Notice also how the faults at the top of the salt dome were misclassified as salt facies, as well as some conformable sediments were misclassified as channel facies.

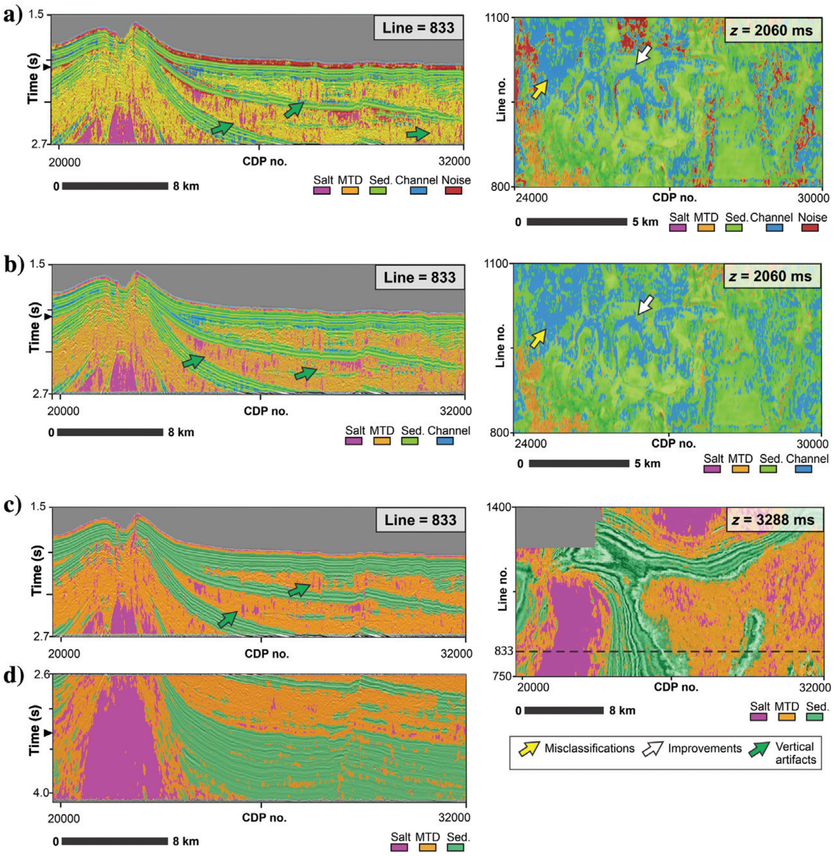

Figure 9. Facies prediction volumes obtained from test 4 after cropping the seismic volume into a shallow and a deep portion. (a) Shallow zone of model 1, (b) shallow zone of model 2, (c) shallow zone of model 3, and (d) deep zone of the model 3. In all of the models, there was a stronger response of the vertical artifacts within the MTDs in the shallow zone. The classifications in the deep portion did not show a considerable difference from the previous tests.

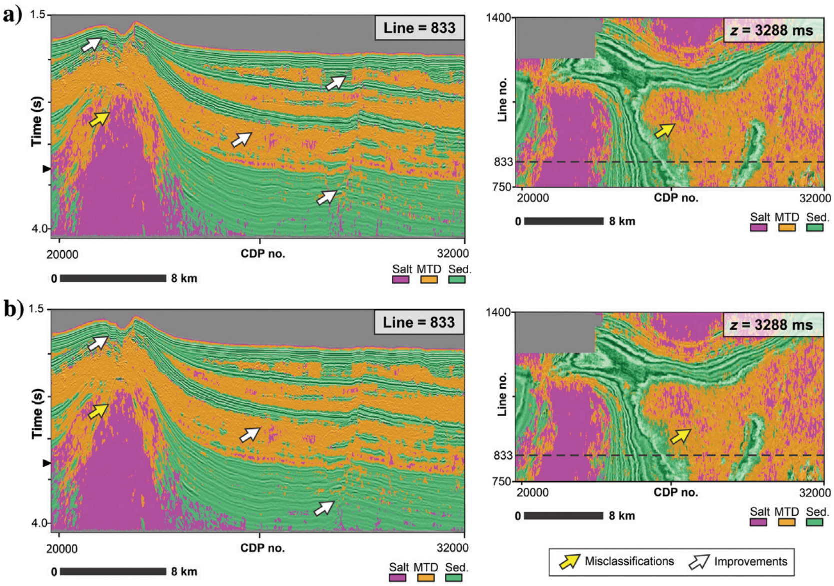

Figure 10. Facies prediction volumes of model 3 in test 5 after: (a) case 1, using k1 calculated with short wavelength and (b) case 2, not using curvature attributes. Notice how in case 1 the misclassifications in the fault zones were diminished, whereas in case 2, they were completely suppressed. In both cases, though, the definition of the salt dome tops was compromised. Note also that there are still some misclassifications of salt facies within the MTDs.

having a higher computational cost, Figure 11a shows that including the fault facies outputted relatively accurate results in the faulted zones with additional misclassification within the conformable sediments and MTD facies.

For the second case, we used two lines and two slices to repick the facies polygons used for training. Contrary to the previous tests, this time, the facies polygons that we picked as conformable sediments enclosed the fault zones present at the top of the first salt dome and in the middle of the seismic section (the right side of Figure 11b). This case had the lowest error value of 0.102 combining the $k1$ (long wavelength), GLCM contrast, envelope, and coherence attributes with a $\boldsymbol{\sigma}$ value equal to 0.2. The results of this classification are shown in Figure 11b. This case successfully suppressed the misclassifications within the normal faults located at the top of the salt domes and in the middle of the seismic section.

For the third case of this test, we classified the salt, MTD, conformable sediments, and a fractured zone related facies (Figure 11c). The classification of this case was performed with the attribute combination of $k1$, envelope, and coherence and $\boldsymbol{\sigma}$ equal to 0.1. This combination corresponded to an error value of 0.239. Despite the MTD intervals of the deeper zones being misclassified as fractured zone facies, the PNN algorithm correctly classified the fractured zones near the salt dome (Figure 11c).

From these three cases, cases 1 and 3 had higher computational costs because they included additional facies. Alternatively, case 2 had the same computation time as the previous classifications of model 3, but it showed the best results (Figure 11b).

Test 7: Final misclassification approach

Prior to this test, the best classification of model 3 was the one obtained from the second case of the previous test 6 with the combination of the $k1$ (long wavelength), GLCM contrast, envelope, and coherence attributes. Although in that case we corrected the misclassifications in the faulted zones, there were some remaining misclassifications between the conformable sediments and the MTD facies that were especially seen at the top of the second salt dome (the right side of Figure 12a). To address these errors, we explored a nonparallelism attribute, known as the dip deviation, and included it within the first case of test 7.

Due to the similarities between the dip deviation and the coherence attributes, we decided to perform the classification using a combination of the $k1$ (long wavelength), GLCM contrast, envelope, and dip deviation attributes. This was done to obtain an unbiased comparison. According to the exhaustive algorithm, this classification had the lowest error value of 0.111 with σ equal to 0.2. The right side of Figure 12a shows a section of the second salt-dome area in the classification volume of the second case from test 6. Here, the highly faulted conformable sediments at the top of the salt dome were misclassified as MTDs. Figure 12b shows the results after using the dip deviation attribute instead of the coherence. Notice that, after using the dip deviation attribute, all of the misclassifications were successfully removed. Nevertheless, inside the salt dome, we noted some misclassifications with a conformable pattern that could be related to multiples and artifacts resulting from the calculation of the dip deviation attribute (Figure 12b).

For the second case of this test, we decided to change the way that we trained the algorithm. This time, we picked the facies polygons in the more complex area of the second salt dome. We performed this classification using the attribute combination of $k2$, envelope, and coherence, with a σ value equal to 0.2 and an associated error value of 0.103. The classifications in the area near the first dome (the left side of Figure 12c) were almost identical to the ones obtained from the second case of test 6, whereas the classifications in the areas near the second salt dome were considerably improved (the right side of Figure 12c). The misclassifications between the conformable sediments and the MTD facies at the top of the salt dome were successfully suppressed, and it was possible to see the continuity of the conformable strata in that region. Also, most of the artifacts inside the salt dome were diminished in comparison to the previous tests.

Discussion

Table 2 reveals that most of the best combinations of attributes included the $k1$-most-positive principal curvature, envelope, and coherence. These results complement the findings from Lubo-Robles et al. (2019), who find that when classifying salt and conformable reflectors, the best combination of attributes is $k1$ and coherence. In our study, because we included more seismic facies in addition to the salt and conformable sediments of Lubo-Robles et al. (2019), it is expected that the algorithm also requires the inclusion of additional seismic attributes for optimal classification results. In our study, it turned out to be the envelope

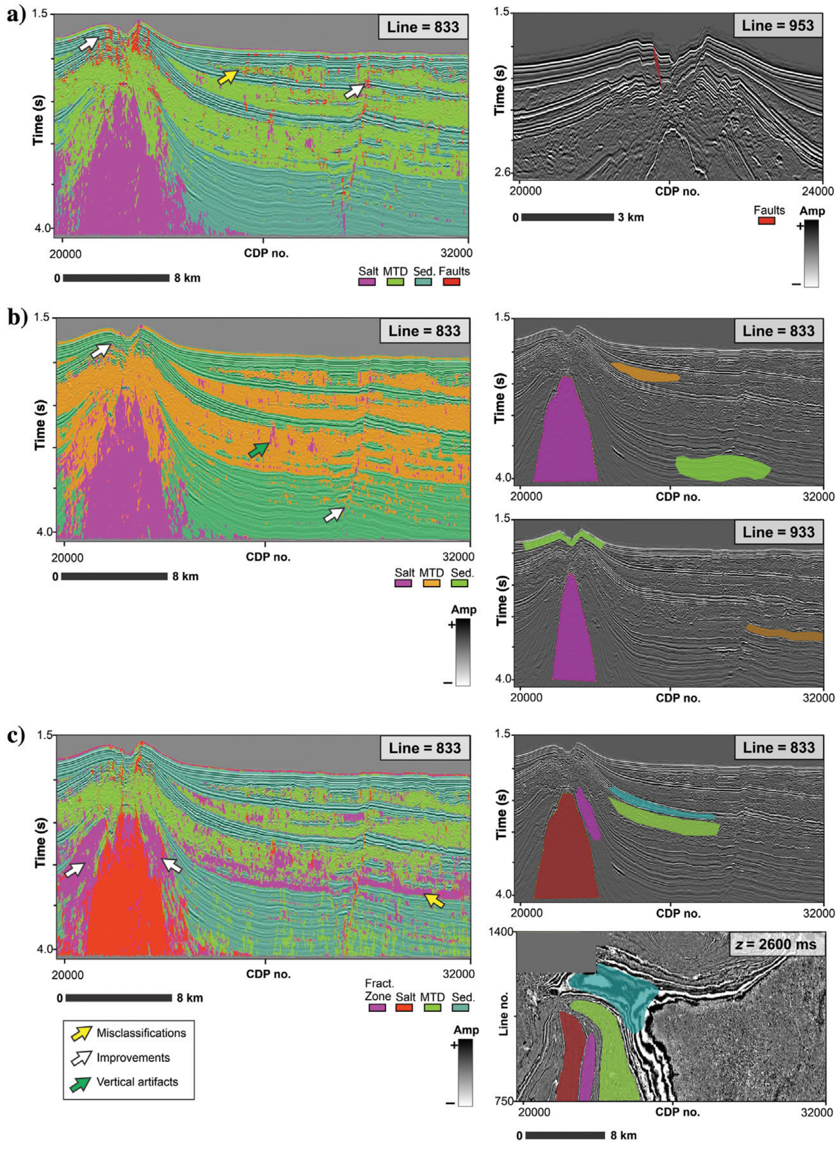

Figure 11. To the right side, are the facies prediction volumes obtained from test 6, and to the left side, there are some samples of facies polygons picked as training for the specific case of the left side. (a) Case 1, after including the fault facies. (b) Case 2, after picking polygons that enclose the fault zones; notice that the new conformable sediment polygons cover a local normal fault and the small faults at top of the first salt dome. (c) Case 3, after including the fractured zone facies that are around the top of the salt domes. In case 1, notice that despite that the faults were correctly classified into their specific facies, this case added additional random misclassifications of the fault facies inside the MTD and conformable sediments facies. In case 2, the misclassifications in the faults were successfully eliminated, and in case 3, the fractured zone was correctly classified but the MTD of the deep interval was misclassified as that facies, too.

attribute, which, contrary to the rest of the seismic attributes used in this study, is not related to any geometric or textural property of the signal, but to the energy of the signal. Table 2 also indicates that the best σ values range from 0.1 to 0.3, which is lower than the best sigma value of 1.9 obtained by Lubo-Robles et al. (2019). This also confirms the mathematics explained by Masters (1995), who indicates that when using higher amounts of training data, the sigma value is expected to decrease. Our results, then, correlated accurately with both studies.

When looking at the first classifications performed in test 1, we realized that the algorithm had limitations for classifying the conformable sediments facies in the deeper zones, which are being incorrectly classified as noise and salt facies (Figure 6). This may be related to the amplitude attenuation effect, which results in the seismic responses of the deeper zones to have lower amplitude values than the seismic responses of the same facies in the shallower zones. Therefore, if the amplitude is naturally compromised, then the envelope attribute is compromised as well, and, as mentioned previously, the envelope is being applied along with the $k1$ and coherence attributes to perform most of the classifications. In this scenario, if the conformable sediments of the deeper zones are composed by continuous and subparallel reflectors but with low amplitude, it is likely that the algorithm will confuse them with the noise facies. Furthermore, if the MTD layers in the deeper zones show low amplitude, then they may also be misclassified as salt facies.

Nevertheless, the results from test 2 indicated how the PNN algorithm could overcome the attenuation of signals with depth and performed better classifications after the training data were doubled. In this test, we noted how the classifications significantly improved, especially in the conformable sediments of the deeper zones for all three models (Figure 7). However, when we used triple the amount of training data for classifying the salt, MTD, and conformable facies, the results were nearly identical compared to when using double the amount of training data. This could be attributed to an overtraining of the algorithm. Hampson et al. (2001) obtain similar results when including more seismic attributes. In their study, the validation error stopped decreasing at some point and the classifications started to overfit the data. These results also support the statements of previous authors (Masters, 1995; West et al., 2002) where PNNs do not require large amounts of training data to have accurate results with low computational costs. For this reason, we continued training our data set using two lines and two slices, to improve the correct classifications, to not overfit the algorithm, and to avoid high computational costs.

After using a larger analysis window when calculating the 3D Kuwahara filter in the seismic attributes, we evidenced a noticeable improvement in the classification of large-scale seismic facies. In the case of small-scale features, though, increasing the 3D Kuwahara filter degraded the classifications, especially the channel facies. Although we were expecting a stronger response of the channel in the seismic attributes and, therefore, in the prediction volumes, the results showed the channel facies being mashed with the other facies. Yet, the noise facies showed the stronger response that we were expecting but extended beyond to the shallow conformable reflectors (Figure 8a). Later in this study, we found that Luo et al. (2002) state that these types of edge-preserving smoothing filters can

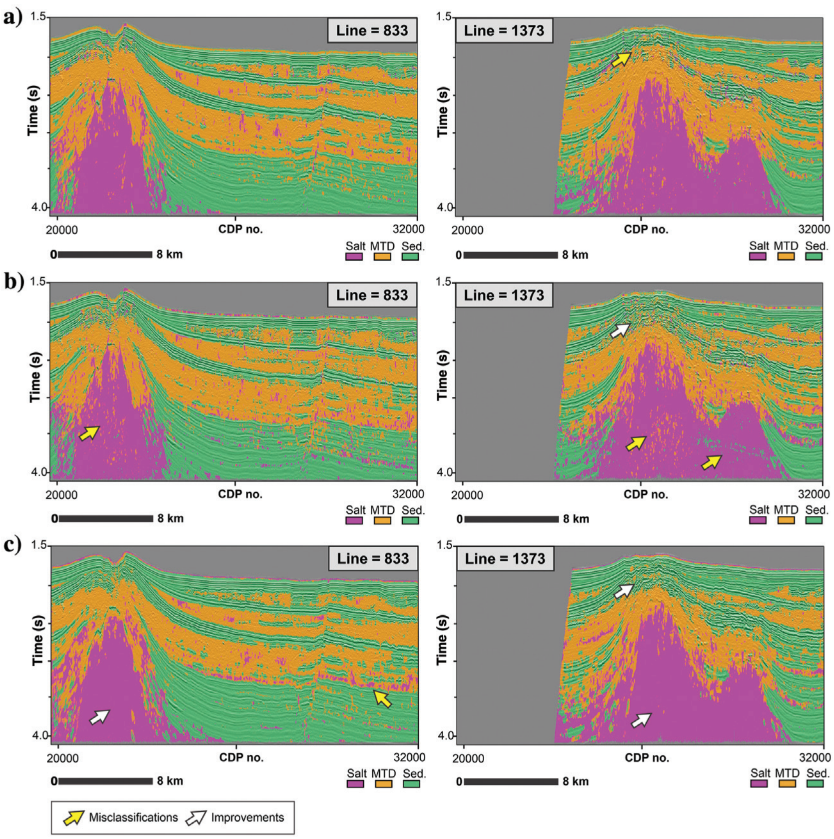

Figure 12. Sections showing the facies predictions in the first salt-dome area to the left and the second salt-dome area to the right. (a) The results of case 2 in test 6 for comparison. In line 1373, notice the misclassifications of the MTD facies within the fractured conformable sediments above the second salt dome top. (b) The results of case 1 in test 7 after replacing the coherence attribute with the dip deviation attribute. Note that the misclassifications at the top of the second salt dome were successfully suppressed; however, this case added misclassifications inside both salt domes. (c) The results of case 2 in test 7 after training in the second salt-dome area. Note that the misclassifications above the second salt dome top were suppressed and there were no artifacts inside either of the salt bodies.

actually suppress geologic features such as channels if their width is smaller than the window size of the filter. Also, Fehmers and Höcker (2003) note that this type of filter not only suppresses random noise, but it can eventually suppress small-scale stratigraphic and structural features as well. Therefore, we suggest classifying small-scale features separately from the classifications of large-scale features, so that when applying the 3D

Table 3. Qualitative impact of each parameter modified on the facies prediction volumes obtained from each case. In the case of the dip deviation attribute, the negative impact cannot be generalized because the conformable artifacts observed in that case are related to the processing task.

Test	Parameter modified	Case	Specific modification	Impact	Commentary
Test 2	Training data	Case 1	Two lines and two time slices for training data	Very positive	Considerably decreased the misclassifications in the deeper part of the seismic volume
		Case 2	Three lines and three time slices for training data	Negative	No additional improvement and higher computational cost
Test 3	Analysis window	—	Larger analysis window for the calculation of the 3D Kuwahara filter	Negative-positive	Negative for the small-scale features and positive for the large-scale features
Test 4	Cropping the volume	Shallow part	Volume cropped into a shallow portion	Negative	Channel better highlighted but considerably increased vertical artifacts in the other seismic facies
		Deep part	Volume cropped into a deep portion	Neutral	Not outstanding difference from previous classifications
Test 5	Seismic attributes selected	Case 1	Curvature attributes calculated with a short wavelength	Relatively positive	Diminished the vertical pattern in the observed artifacts and in the faults, but compromised the definition of the tops of the salt domes
		Case 2	Not using curvature attributes	Relatively positive	Suppressed the vertical pattern in the observed artifacts and in the faults, but compromised the definition of the tops of the salt domes
Test 6	Seismic facies included	Case 1	Including fault facies	Negative	Classified beyond the fault planes, added random misclassifications, and increased the computational cost
	Training data	Case 2	Picking polygons enclosing the faulted areas	Very positive	Suppressed the misclassifications in the faults and did not increase the computational cost
	Seismic facies included	Case 3	Including fractured zone facies	Relatively positive	Correctly classified the highly fractured areas near the salt dome top but increased the misclassifications in the MTD of the deep part
Test 7	Seismic attributes selected	Case 1	Including the dip deviation attribute	Relatively negative*	Suppressed the misclassifications between the conformable sediments at the top of the second salt dome and the MTD facies. Substantially increased artifacts inside the salt domes
	Training data	Case 2	Picking polygons in the challenging zones near the salt #2	Positive	Considerably decreased misclassifications between the faulted conformable sediments and the MTD facies. Showed less artifacts inside the salt domes

Note: *As the dip deviation attribute is directly related to reflector parallelism, it may fail when classifying areas with conformable artifacts or multiples. We should not discard this attribute for future classifications, as it did show improvements, for example, in faulted zones.

Kuwahara filter, the interpreter can use the analysis window accordingly. We highly recommend following the advice of Qi et al. (2015), who apply larger 3D Kuwahara windows when performing classifications of seismic facies related to large-scale features but not when classifying small-scale features.

When cropping the seismic volume in test 4, the classifications in the shallow zone for the three models exhibited stronger responses in the vertical artifacts, whereas the only change in the deep zone was that what we interpreted as fractured zones were classified as MTD instead of salt facies in comparison with the previous tests. A noteworthy aspect of this test was the channel and the noise layer in model 1, which were strongly classified into their respective facies. In other words, the algorithm showed stronger responses for the correct interpretations and for the artifacts and misclassifications. One explanation for the results of this test may be an increase in the confidence of the algorithm, which is calculating higher probabilities for the predominant facies by having the same amount of training data with a smaller volume to classify.

In general, we saw that despite the channel and the noise layer having been well classified into their respective facies, there were some other areas that were consistently misclassified as those facies. We tried to correct those misclassifications through many different tests. However, the prediction volumes of these small-scale related facies continued to show the same misinterpretations with no signs of improvement, contrary to the model with only large-scale features, which progressively generated better results. These results may be related to geologic and/or geophysical reasons. One reason would be the possible presence of turbiditic stacked channels. Further analysis with complementary well-log data would be needed to confirm or discard whether the misclassified channel facies are in fact correctly classified stacked channels systems. Another reason could be due to the similar seismic attribute responses of those seismic facies, making it difficult for the algorithm to differentiate between them. This would imply a limitation of this technique when this kind of situation arises, and supplementary research would be necessary to explore other seismic attributes that allow for a better discrimination of those facies.

In addition, in the previous tests, we recognized some vertical artifacts that were classified as salt facies. We tried to address these errors in tests 5 and 6. Regarding the specific origin of these vertical artifacts, we considered that they may be related to the following reasons: (1) It is well known that, for normal faults, there are high positive curvature responses at the edge of the footwalls and high negative curvature responses at the edge of the hanging walls (Klein et al., 2008). The similar responses between the footwalls and the salt domes in the $k1$ attribute volume explained why these artifacts are in the faulted zones and why they were misclassified as salt facies. (2) In the case of the vertical artifacts observed inside of the MTDs and less obvious in the other facies, we considered that they may be related to the processing task. When reviewing the seismic amplitude volume, these last artifacts coincide with patterns similar to those observed at the very top of the salt domes. Therefore, this implies very high positive values in the $k1$ attribute volume that lead to misclassifying those areas as salt facies.

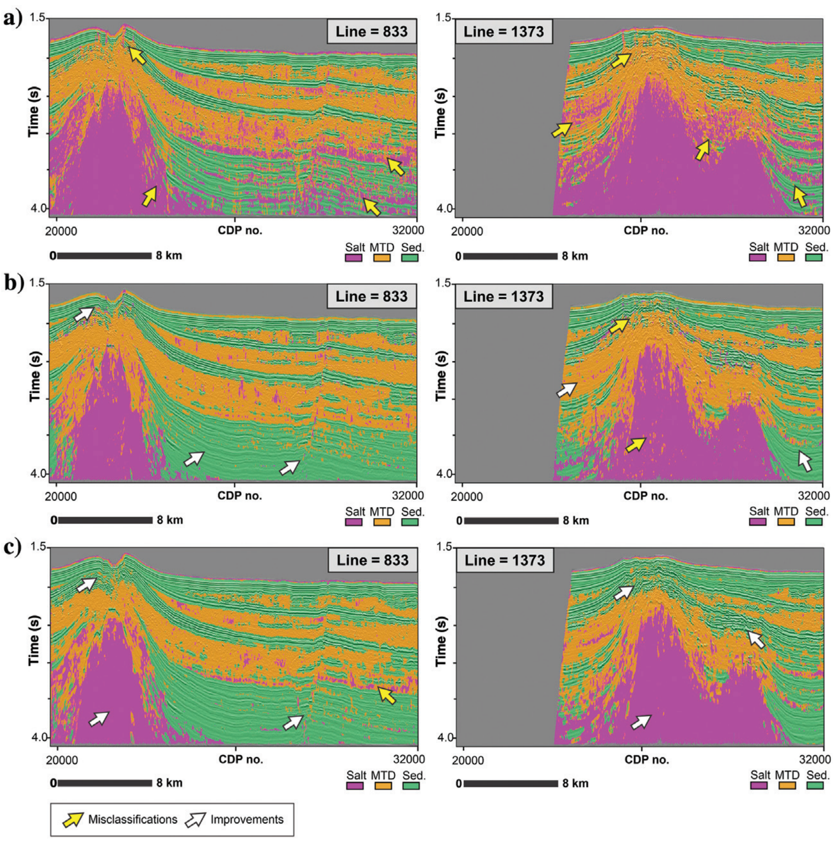

Figure 13. Evolution of the seismic facies classification for model 3, from the very first one to the last one. Note the progressive improvement after including the geoscientist criteria to change the initial parameters. To the left, there are the sections showing the first salt-dome area, and to the right, there are the sections showing the second salt-dome area. (a) The results of model 3 in test 1: Note the misclassifications in the fault zones and in the deep portion of the volume. (b) The results of model 3 in test 6 after picking new polygons enclosing the fault areas. In this classification, we also used double the amount of training data. Note that the misclassifications in the fault zones and in the deep portion of the volume were corrected. (c) The results of case 2 in test 7, after picking all of the facies polygons in the more complex area of the second salt dome. Notice the correction in the classification of the conformable sediments' facies in the top of the second salt dome.

In the case of test 5, we could see that by changing the wavelength used to calculate the curvature attribute, it was possible to diminish the vertical pattern from the artifacts previously discussed. Using a short-wavelength curvature instead of a long-wavelength curvature helped to decrease the strong response of those vertical artifacts, while not using curvature attributes completely suppressed them from the faulted zones. However, in both cases, the definition of the salt dome tops was affected. In test 6, we found another method for suppressing the vertical artifacts from the faulted zones without compromising the definition of the salt dome tops. These results showed that by only changing the way we picked the facies polygons and enclosing the faults inside those facies polygons, it helped to successfully eliminate the misclassifications in the faulted zones (Figure 11b). We obtained similar results in test 7, in which we changed from picking in the easiest portions of the first salt dome to picking in the most challenging portions of the second salt dome. With that final test, we were able to correct the misclassifications in the highly faulted conformable sediments at the top of the second salt dome and to obtain stronger responses inside both salt domes (Figure 12c). These results allowed us to recognize the importance of the definition of the facies polygons because they can accomplish considerably better results.

The other classifications performed in tests 6 and 7 reiterated how the processing of the data set has an impact on the classification volumes. When attempting to classify salt, MTD, conformable sediments, and fractured zone facies, the deeper intervals of MTD strata were misclassified as fractured zone facies. These results were despite the promising results shown by the PNN algorithm when classifying the fractured zone into its corresponding facies (Figure 11c). This must be related to lower amplitudes present within the MTD intervals of the deeper zones. However, using the dip deviation attribute helped to correct the misclassifications in the conformable facies of the top of the second salt dome (Figure 12b). Nevertheless, it also added conformable artifacts inside the salt domes, probably due to multiples with a conformable pattern. In this final case, we cannot generalize that the dip deviation may not work and discard it for future facies predictions. If there are conformable artifacts or multiples, it is most likely that this attribute may fail in those zones because it is directly related to reflector parallelism.

Overall, despite PNN being an early reconnaissance tool, with the computation capabilities available nowadays, it demonstrated to be a great tool to integrate considerable amounts of information and perform multiattribute analysis at a scale that would be overwhelming for an interpreter applying only conventional

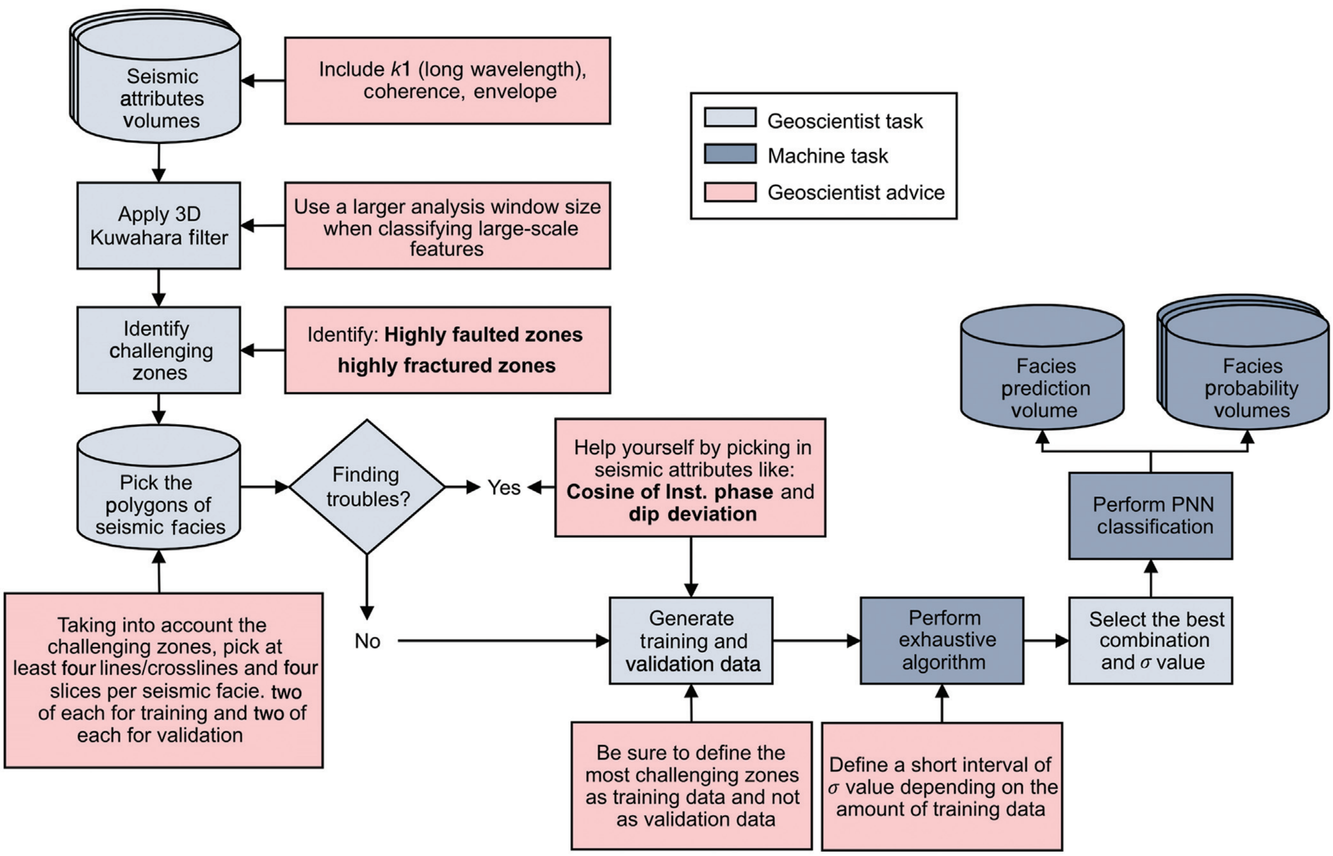

Figure 14. Final workflow including the geoscientist's advice to obtain better classifications when using PNNs for seismic facies classifications.

interpretation. Still, a limitation identified when applying PNN as a multiattribute analysis technique arises when two different seismic facies have similar to exactly the same seismic attributes response, therefore leading the PNN algorithm to classify them as if they were the same. We noticed that when the method misclassified conformable sediments as noise or channel facies, or MTDs as salt. These kinds of situations should be addressed with caution by the interpreter to determine the optimal way to proceed, and we reiterate the necessity of having a geoscientist to ground truth the machine learning algorithm's interpretation.

Table 3 summarizes the qualitative impact of each parameter changed on the seismic facies classifications performed in each test. Figure 13 shows the progressive evolution from the very first classification to the last one of the prediction volumes of the large-scale facies of model 3. This last figure clearly illustrates the importance of including the geoscientist's insight to obtain better results. Finally in Figure 14, we compiled all of the lessons learned, and we proposed a new workflow that will help as a guide for future interpreters interested in applying PNNs for seismic facies classification. The geoscientist's criteria are quite important because we can infer where it is going to be more challenging for the algorithm to classify into the specific seismic facies. In this sense, the most important step included in this new workflow is to first recognize the most geologically complex areas and then pick the training facies polygons taking them into account. Incorporating this geologic insight will help the algorithm to generate more accurate results since the beginning.

Finally, we suggest the application of this technique and workflow as a great option for regional or basin scale studies, especially when multiple seismic data sets are required and the amount of conventional interpretation needed would be considerable. The interpreter is not only expected to reduce interpretation times and computational cost, but also to get a reliable and accurate understanding of the direction of movements of MTDs, spatial distribution and geometry of salt structures, and volumetric calculations of channels, or to use all those outcomes to improve, for example, velocity models as well.

Conclusion

PNNs demonstrated to be an accurate machine learning technique for supervised seismic facies classification, showing remarkable accurate results when classifying large-scale features and showing promising but limited results when classifying small-scale features. The exhaustive algorithm indicated that, for future classifications of the seismic facies addressed here, it is important to include the $k1$-most-positive principal curvature, envelope, and the coherence attributes. This is because they consistently ranked among the highest contributing attributes. Also, when using huge amounts of data, it is not necessary to consider large intervals for the σ value because we saw that the value for all of the best combinations varied between 0.1 and 0.3.

In this study, we highlighted the importance of including geologic insight to progressively obtain better results. This was first done by understanding the origins of the misclassifications then by helping the algorithm to overcome them through the modification of initial parameters. The effect of amplitude attenuation was corrected by adding more training data, whereas the vertical artifacts were diminished by changing the way we calculate the curvature attributes. Finally, the misclassifications in the faulted zones and conformable sediments were corrected by changing the way of picking the facies polygons used for training. It is important to note that all of these tasks were controlled and altered by the geoscientist, not the algorithm.

In addition, we showed how the processing artifacts can highly impact on the final classification volumes. Attenuation of energy can cause conformable sediments to have responses similar to the noise present near the seafloor. The vertical artifacts seen in the faulted zones and inside of the MTDs have responses similar to the salt domes; therefore, they were misclassified as salt facies. We also saw that conformable artifacts may have an impact on attributes that measure reflector parallelism, such as the dip deviation attribute, and they can be prone to misclassification. We can help the algorithm's training by changing the preselected attributes or by altering the way that they are calculated. However, if those artifacts persist, we must understand that those are inherent limitations that the algorithm is unable to overcome. Therefore, it is not necessary to further try to polish these results unless there is a better processed seismic survey available.

In conclusion, we have proposed a new workflow that incorporates the best practices for applying PNNs. Although the selection of seismic attributes is crucial to maximize the differences between seismic facies, we also demonstrated that the generation of facies polygons is just as essential. For that reason, we consider that the most important step in this new workflow is to use the geoscientist's criteria to recognize the most geologically complex areas and create the training polygons within those regions. Finally, we consider the application of this workflow to be of great interest when intended for regional or basin-scale analysis to reduce interpretation times and computational cost, but also, and most importantly, to get reliable results that allow for a better understanding of the spatial distribution of the seismic facies of interest.

Acknowledgments

We would like to thank the U.S. Geological Survey (USGS) and the Bureau of Ocean Energy Management for providing the data set. Also, we thank the sponsors of the Attribute Assisted Seismic Processing and Interpretation consortium for their support and to Schlumberger for providing the Petrel License to the University of Oklahoma. Thanks to the members of the SDA

Research Group at the University of Oklahoma for their valuable comments, especially to J. Chenin, J. Tellez, and D. Lubo.

Data and materials availability

Data associated with this research are available and can be accessed via the following URL: https://walrus.wr.usgs.gov/namss/survey/b-43-91-tx/. Note: A digital object identifier (DOI) linking to the data in a general or discipline-specific data repository is strongly preferred.

References

Al Dossary, S., and K. J. Marfurt, 2006, 3D volumetric multispectral estimates of reflector curvature and rotation: Geophysics, **71**, no. 5, P41–P51, doi: 10.1190/1.2242449.

Barnes, A. E., and K. J. Laughlin, 2002, Investigation of methods for unsupervised classification of seismic data: 72nd Annual International Meeting, SEG, Expanded Abstracts, 2221–2224, doi: 10.1190/1.1817152.

Chopra, S., and K. J. Marfurt, 2007a, Seismic attributes for prospect identification and reservoir characterization: SEG.

Chopra, S., and K. J. Marfurt, 2007b, Curvature attribute applications to 3D surface seismic data: The Leading Edge, **26**, 404–414, doi: 10.1190/1.2723201.

Chopra, S., and K. J. Marfurt, 2010, Integration of coherence and volumetric curvature images: The Leading Edge, **29**, 1092–1107, doi: 10.1190/1.3485770.

Chopra, S., and K. J. Marfurt, 2011, Interesting pursuits in seismic curvature attribute analysis: CSEG Recorder, **36**, 40–50.

Chopra, S., and K. J. Marfurt, 2018, Seismic facies classification using some unsupervised machine-learning methods: 88th Annual International Meeting, SEG, Expanded Abstracts, 2056–2060, doi: 10.1190/segam2018-2997356.1.

Coléou, T., M. Poupon, and K. Azbel, 2003, Unsupervised seismic facies classification: A review and comparison of techniques and implementation: The Leading Edge, **22**, 942–953, doi: 10.1190/1.1623635.

Deriche, M., 2016, Robust salt-dome detection using the ranking of texture-base attributes: Applied Geophysics, **13**, 449–458, doi: 10.1007/s11770-016-0569-6.

Di, H., Z. Li, H. Maniar, and A. Abubakar, 2019, Seismic stratigraphy interpretation via deep convolutional neural networks: 89th Annual International Meeting, SEG, Expanded Abstracts, 2358–2362, doi: 10.1190/segam2019-3214745.1.

Donovan, A. D., J. M. Casey, D. I. Sanabria, D. K. Willis, and D. A. Stauber, 2003, Composite sequences, seismic facies, and reservoir distributions in the Dianna Hoover Basin: Gulf of Mexico: Presented at the Annual Convention, AAPG.

Fehmers, G. C., and C. F. W. Höcker, 2003, Fast structural interpretation with structure-oriented filtering: Geophysics, **68**, 1286–1293, doi: 10.1190/1.1598121.

Galloway, W. E., 2008, Depositional evolution of the Gulf of Mexico sedimentary basin, *in* A. D. Miall, ed., Sedimentary basins of the world: Elsevier, **5**, 505–549.

Gao, D., 2003, Volume texture extraction for 3D seismic visualization and interpretation: Geophysics, **68**, 1294–1302, doi: 10.1190/1.1598122.

Hampson, D. P., J. S. Shuelke, and J. A. Quirein, 2001, Use of multiattribute transforms to predict log properties from seismic data: Geophysics, **66**, 220–236, doi: 10.1190/1.1444899.

Kim, Y., R. Hardisty, and K. J. Marfurt, 2019, Multivariate attribute selection in seismic facies classification: 89th Annual International Meeting, SEG, Expanded Abstracts, 2258–2262, doi: 10.1190/segam2019-3216101.1.

Klein, P., L. Richard, and H. James, 2008, 3D curvature attributes: A new approach for seismic interpretation: First Break, **26**, 105–111, doi: 10.3997/1365-2397.26.1118.27953.

La Marca-Molina, K., 2020, Seismic attribute optimization with unsupervised machine learning techniques for deepwater seismic facies interpretation: Users vs machines: M.S. thesis, University of Oklahoma.

Leiphart, D. J., and B. S. Hart, 2001, Comparison of linear regression and a probabilistic neural network to predict porosity from 3-D seismic attributes in lower Brushy Canyon channeled sandstones, southeast New Mexico: Geophysics, **66**, 1349–1358, doi: 10.1190/1.1487080.

Liu, M., W. Li, M. Jervis, and P. Nivlet, 2019, 3D seismic facies classification using convolutional neural network and semi-supervised generative adversarial network: 89th Annual International Meeting, SEG, Expanded Abstracts, 4995–4999, doi: 10.1190/segam2019-3216797.1.

Lubo-Robles, D., T. Ha, S. Lakshmivarahan, and K. J. Marfurt, 2019, Supervised seismic facies classification using probabilistic neural networks: Which attributes should the interpreter use? 89th Annual International Meeting, SEG, Expanded Abstracts, 2273–2277, doi: 10.1190/segam2019-3216841.1.

Lubo-Robles, D., T. Ha, S. Lakshmivarahan, K. J. Marfurt, and M. J. Pranter, 2021, Exhaustive probabilistic neural network for attribute selection and supervised seismic facies classification: Interpretation, **9**, no. 2, T421–T441, doi: 10.1190/INT-2020-0102.1.

Luo, Y., M. Marhoon, S. Al Dossary, and M. Alfaraj, 2002, Edge-preserving smoothing and applications: The Leading Edge, **21**, 136–158, doi: 10.1190/1.1452603.

Masters, T., 1995, Advanced algorithms for neural networks: A C++ sourcebook: John Wiley & Sons Inc.

Mercado-Herrera, V., B. Russell, and A. Flores, 2006, Neural networks in reservoir characterization: The Leading Edge, **25**, 402–411, doi: 10.1190/1.2193208.

Miller, P., S. Dasgupta, and D. Shelander, 2012, Seismic imaging of migration pathways by advanced attribute analysis, Alaminos Canyon 21, Gulf of Mexico: Marine and Petroleum Geology, **34**, 111–118, doi: 10.1016/j.marpetgeo.2011.09.005.

Nixon, L., E. Kazanis, and S. Alonso, 2014, Deepwater Gulf of Mexico: U.S Department of the Interior, Bureau of Ocean Energy Management, Gulf of Mexico OCS Region.

Posamentier, H. W., and V. Kolla, 2003, Seismic geomorphology and stratigraphy of depositional elements in deep-water settings: Journal of Sedimentary Research, **73**, 367–388, doi: 10.1306/111302730367.

Posamentier, H. W., and O. J. Martinsen, 2011, The character and genesis of submarine mass-transport deposits: Insights from outcrop and 3D seismic data, *in* R. C. Shipp, P. Weimer, and H. W. Posamentier, eds., Mass-transport deposits in deepwater settings: SEPM Special Publication, **95**, 7–38.

Pramanik, A. G., V. Singh, R. Vig, A. K. Srivastava, and D. N. Tiwary, 2004, Estimation of effective porosity using geostatistics and multiattribute transforms: A case study: Geophysics, **69**, 352–372, doi: 10.1190/1.1707054.

Putri, I. A., A. Rubaiyn, and A. Robby-Rizaldi, 2018, Probabilistic neural network (PNN) for tight sand reservoir characterization: International Geophysical Conference, CPS/SEG, Expanded Abstracts, 1260–1263, doi: 10.1190/IGC2018-307.

Qi, J., M. Cahoj, A. AlAli, L. Li, and K. J. Marfurt, 2015, Segmentation of salt domes, mass transport complexes on 3D seismic data volumes using Kuwahara windows and multiattribute cluster analysis: 85th Annual International Meeting, SEG, Expanded Abstracts, 1821–1825, doi: 10.1190/segam2015-5876831.1.

Qi, J., T. Lin, T. Zhao, F. Li, and K. J. Marfurt, 2016, Semisupervised multiattribute seismic facies analysis: Interpretation, **4**, no. 1, SB91–SB106, doi: 10.1190/INT-2015-0098.1.

Qi, J., and K. J. Marfurt, 2019, Nonparallelism attributes and data adaptive Kuwahara image processing: 89th Annual International Meeting, SEG, Expanded Abstracts, 1858–1862, doi: 10.1190/segam2019-3216022.1.

Roksandić, M. M., 1978, Seismic facies analysis concepts: Geophysical Prospecting, **26**, 383–398, doi: 10.1111/j.1365-2478.1978.tb01600.x.

Roy, A., B. L. Dowdell, and K. J. Marfurt, 2013, Characterizing a Mississippian tripolitic chert reservoir using 3D unsupervised and supervised multiattribute seismic facies analysis: An example from Osage County, Oklahoma: Interpretation, **1**, no. 2, SB109–SB124, doi: 10.1190/INT-2013-0023.1.

Sarkar, S., K. J. Marfurt, B. Ferrero-Hodgson, and R. M. Slatt, 2008, Attribute expression of mass transport deposits in an intraslope basin — A case study: 78th Annual International Meeting, SEG, Expanded Abstracts, 958–962, doi: 10.1190/1.3063797.

Specht, D. F., 1988, Probabilistic neural networks for classification mapping, or associative memory: Proceedings of the IEEE International Conference on Neural Networks, 525–532.

Specht, D. F., 1990, Probabilistic neural networks: Neural Networks, **3**, 109–118, doi: 10.1016/0893-6080(90)90049-Q.

Subrahmanyam, D., and P. H. Rao, 2008, Seismic attributes — A review: Proceedings of the 7th International Conference and Exposition on Petroleum Geophysics.

Sullivan, M., G. Jensen, F. Goulding, D. Jennette, L. Foreman, and D. Stern, 2000, Architectural analysis of deep-water outcrops: Implications for exploration and development of the Diana sub-basin, Western Gulf of Mexico, *in* P. Weimer, ed., Deep-water reservoirs of the world: SEPM Society for Sedimentary Geology, 1010–1031.

Taner, M. T., F. Koehler, and R. E. Sheriff, 1979, Complex seismic trace analysis: Geophysics, **44**, 1041–1063, doi: 10.1190/1.1440994.

Verma, S., A. Roy, R. Perez, and K. J. Marfurt, 2012, Mapping high frackability and high TOC zones in the Barnett Shale: Supervised probabilistic neural network vs unsupervised multi-attribute Kohonen SOM: 82nd Annual International Meeting, SEG, Expanded Abstracts, doi: 10.1190/segam2012-1494.1.

Waldeland, A. U., A. C. Jensen, L. J. Gelius, and A. H. Schistad-Solberg, 2018, Convolutional neural networks for automated seismic interpretation: The Leading Edge, **37**, 529–537, doi: 10.1190/tle37070529.1.

Weimer, P., and R. M. Slatt, 2006, Petroleum geology of deepwater settings: AAPG Studies in Geology.

West, B. P., S. R. May, J. E. Eastwood, and C. Rossen, 2002, Interactive seismic facies classification using textural attributes and neural networks: The Leading Edge, **21**, 1042–1049, doi: 10.1190/1.1518444.

Wrona, T., I. Pan, R. L. Gawthorpe, and H. Fossen, 2018, Seismic facies analysis using machine learning: Geophysics, **83**, no. 5, O83–O95, doi: 10.1190/geo2017-0595.1.

Zhao, T., V. Jayaram, A. Roy, and K. J. Marfurt, 2015b, A comparison of classification techniques for seismic facies recognition: Interpretation, **3**, no. 4, SAE29–SAE58, doi: 10.1190/INT-2015-0044.1.

Zhao, T., F. Li, and K. J. Marfurt, 2018, Seismic attribute selection for unsupervised seismic facies analysis using user-guided data-adaptive weights: Geophysics, **83**, no. 2, O31–O44, doi: 10.1190/geo2017-0192.1.

Zhao, T., S. Verma, J. Qi, and K. J. Marfurt, 2015a, Supervised and unsupervised learning: how machines can assist quantitative seismic interpretation: 85th Annual International Meeting, SEG, Expanded Abstracts, 1734–1738, doi: 10.1190/segam2015-5924540.1.

Diana Salazar-Florez received a B.S. (2021) in geology from Universidad Industrial de Santander, where she was an active member of the AAPG and EAGE student chapters. During her senior year, she worked as a geology intern for Repsol Colombia; later, she went to the University of Oklahoma as an exchange student and as a research intern under the advisory of Heather Bedle. She is a current member of SEG, and her research interests include seismic interpretation, 3D seismic attributes, and application of machine learning in geosciences.

Heather Bedle received a B.S (1999) in physics from Wake Forest University and then worked as a systems engineer in the defense industry. She later received master's and doctorate degrees from Northwestern University. After nine years of working with Chevron, she instructed at the University of Houston for two years and has been assistant professor at the University of Oklahoma since 2018. Her primary research interests merge seismic interpretation, rock physics, attribute analysis, and machine learning.